CARMA Memorandum Series #62

CARMA Summer School 2013

Melvyn Wright, Marc Pound, Dick Plambeck, John Carpenter, Nikolaus Volgenau, Doug Friedel, Melodie Kao, Gina Duggan, Ben Tofflemire, Melissa Louie, Rosalie McGurk, Hsi-An Pan, Sandy Liss, Emma Yu, Jesus Rivera, Stephen Clouse, Michiko Umei, Alfred Tiley, Moumita Aich, Anna Miotello, Shuo Kong, Nina Van der Pyl, Arnab Dhabal, Sam Kim, Yixian Cao, Katherine de Kleer, Natalie Butterfield

October 21, 2013

ABSTRACT

The 7th CARMA Summer School was held at the observatory at Cedar Flat 2013 on July 28-Aug 3, 2013 with 21 students from Berkeley, Caltech, Illinois, Maryland, U. Wisconsin, SUNY, UC Santa Cruz, U. Virginia, U. Texas, Rutgers U., Hokkaido University, Leiden Observatory, Nobeyama Observatory, Oxford, U. Iowa, U. Florida, Bristol, U. KwaZulu-Natal, and PUC Chile. During the school, students formed small teams and designed and obtained their own observations, in consultation with the instructors. Using both science subarrays, students observed star-forming regions, YSOs and outflows, planets atmospheres and polarization, an M-dwarf star, nearby galaxies, a high-z galaxy, and galaxy clusters. At the end of the week, the students gave short presentations on their results. In this memo we collect together some of the results from the student projects.

1. Introduction

The 7th CARMA Summer School was held at the observatory at Cedar Flat 2013 on July 28-Aug 3, 2013 with 21 students and 6 instructors. This year had strong international participation with 8 students from non-US insitutions. As in previous years, the school had the use of the telescope for the week. The array was in the most compact E-configuration. During the school the students had their own observing projects which they worked on during the week as well as attending lectures and demonstations. Each of the student projects had 5-6 hours of telescope time and the students controlled the telescope for their own projects. The students took the observations, reduced and analyzed the data, and presented the results.

On the first day the students learned how to select suitable observing projects for the CARMA telescope. The introductory lectures covered the characteristics of the telescope, instrumentation, and observing techniques which taught the students to:

- select suitable astronomical sources for observing.
- select the observing frequency, spectral lines to be observed.
- evaluate angular resolution, velocity resolution and sensitivity needed.
- select the correlator setup and calibrations needed.
- prepare an observing script to define the observing procedure at the telescope.
- make the observations

During the rest of the week, the lectures and demonstrations covered the theory and techniques used for millimeter wavelength aperture synthesis and for the CARMA array, and more detailed lectures on the hardware and software. As they worked on their projects the students learned how to:

- schedule the telescope effectively.
- calibrate the data.
- make images.
- identify and fix problems that set off the alarm.
- analyze and present the results.

On Friday the students made 10-15 minute presentations and we discussed the results. In all, a very satisfying week seeing all the enthusiasm and so many exciting projects from initial planning and observations, to analysis and results.

2. The CARMA Telescope

The CARMA telescope is an aperture synthesis array, typically operating as two independent subarrays of 15 and 8 antennas, respectively. In the CARMA-15 subarray, there are two receiver bands, 3 mm and 1 mm, and the spectral line correlator. A basic aperture synthesis observation makes an image the size of the the primary beam ($\lambda/D \sim 1'$ at 100 GHz; $0.5'$ at 230 GHz) with a resolution corresponding to the maximum separations of the antennas. During the Summer School, CARMA-15 was in the E configuration, with an angular resolution $\sim 10''$ at 100 GHz, and $\sim 5''$ at 230 GHz. The CARMA-8 subarray of eight 3.5m antennas was in the SL configuration for continuum-only projects at 30 GHz (primary beam $\sim 11'$; resolution $\sim 2'$) and 90 GHz (primary beam $\sim 3.6'$; resolution $\sim 40''$). The CARMA-8 correlator produces 7 GHz of continuum data. All antennas can be combined into a single 23-element array, CARMA-23, with 4 GHz of correlator bandwidth.

It's best to observe a strong enough source that one can make an image during the school, rather than a detection project, then the effects of different imaging techniques can be explored. The most convenient source size is one which is smaller than the size of the primary beam when only one pointing is needed. Larger sources can be imaged by time-sharing the pointing of the antennas (mosaicing), at the cost of lowered sensitivity.

The sensitivity is determined by the system noise (receivers plus atmosphere), the bandwidth (or velocity resolution), and the observing time. The atmosphere is usually not so good for 1 mm observations in the summer (although a couple 1 mm projects were run this year), for sources which are at low declinations that must be observed through more of the atmosphere, so select a bright source which is high in the sky and can be observed at 3 mm or 1 cm is preferred. Not all the projects that the students wanted to do satisfied these these conditions, so a final list of projects from those proposed was selected on the first day of the school. Students grouped themselves into small teams to work on the selected projects.

2.1. Logistics

Because this is a hands-on school, all lectures and demonstrations were held in the control building and at the telescopes at Cedar Flat. Mel, Marc, Dick, Doug, and 16 of the students stayed in the "Noren" group campground, about 1.5 miles from the control room, and near the antenna pads for the A-configuration. Those who camped avoided the hassle of driving up and down the mountain each day and had a wonderful opportunity to fall asleep under a star-filled and moonless sky each night. The other students stayed in the dorm and cottage at OVRO. Delicious breakfasts, lunches, and dinners were provided at the observatory, prepared by Sarah Landry and Barbara Marzano. Mary Daniel adroitly handled all the accomodations, making sure every one had a place to rest their weary heads at the end of the long days. We organized a hike to Second Lake on Saturday.

3. Comparison of ^{12}CO$(1-0)$ and ^{13}CO$(1-0)$ line emissions of NGC 6764

Yixian Cao, Gina Duggan, Jesus Rivera

3.1. Introduction

Nuclear starburst galaxies are interesting because they are in an intense state of high star formation rate. NGC 6764 is an active barred spiral galaxy and is classified as a low-ionization nuclear emission-line region. The study of NGC 6764 is further motivated because of the composite nature of its nucleus hosting both a starburst and an AGN (Leon et al. 2007). The motivation for observing this specific object with CARMA was twofold: the first motivation was to observe an object with a previously detected CO emission so as to have data to reduce with MIRIAD; and the second motivation was to calculate the ratios of the detected CO lines to gain insight into some of the physical properties of the galaxy. We observed NGC 6764 for ^{12}CO, ^{13}CO, and C^{18}O line emissions.

3.2. Observations and Data Reduction

We observed the NGC 6764 using a 15 antenna compact configuration (E configuration) at CARMA. On July 30, 2013 the center 33 arcseconds of NGC6764 was observed for 6.7 hours at $\alpha = 19:08:16.3$ and $\delta = +50:56:00$ Dec. The calibration objects used were: 2038+513 for gain, 1927+739 for pass band, and mwc349 for flux. The galaxy has expected CO line widths of $\sim$ 400 km/s, which required us to approximately have 10 km/s resolution (Leon et al. 2007). As a result our observation script consisted of three 250 MHz for the spectral windows and five 500 MHz continuum windows for each the Lower Side-Band and the Upper Side-Band, with the local oscillator frequency set at 109.095 GHz. We observed ^{12}CO$(1-0)$, ^{13}CO$(1-0)$, and $C^{18}O(1-0)$ spectral lines at 115.27, 110.20, and 109.78 GHz respectively. The $C^{18}O(1-0)$ spectral line was not measured.

The bulk of the data reduction was done using John Carpenter's script for reducing MIRIAD data. However, parameters were changed so the script would run according to our needs. In order to get a cleaner signal, antennas 1, 2 , 8, 9 and 10 were removed. In addition, we flagged points as outliers based on phase and amplitude plots from the gain and passband calibrators.

3.3. Results and Discussion

3.3.1. ^{12}CO$(1-0)$*Emission*

The integrated intensity map and velocity field of ^{12}CO$(1-0)$ are represented in Figure 1. The ^{12}COemission is distributed mostly on a scale of $40''$. The emission in the center is very strong. The emission is also extend along the bar to the northeast and southwest. The velocity field of ^{12}CO$(1-0)$ shows the northeastern arm is redshifted while the southwestern arm is blueshifted with respect to the center.

Figure 2 shows the moment 0 map again, but this time using contours. This figure shows five positions: center (A), middle right (B), far right (C), middle left (D), upper left (E). The spectra at each of these positions are shown in Figure 3. These same five positions are used to analyze the ^{13}CO$(1-0)$ emission line in section 3.3.2.

The spectra displayed in Figure 3 is roughly a Gaussian centered at $\sim$2400 km/s as we would expect since the recorded velocity of NGC 6764 is 2420 km/s (Eckart et al. 1991). The width of the spectra becomes narrower as the position becomes more removed from the center of the object. The spectra from the center (position A) has a width of $\sim$300 km/s. Position B and D are about 2 arcseconds away from the center and have a width of $\sim$200 km/s. Position E looks roughly the same width as the spectra from position B and D, but position C (which is about 9 arcseconds from the center) is very narrow with width $\sim$100 km/s.

3.3.2. ^{13}CO$(1-0)$ *Emission*

In Figure 4 we show the results of ^{13}CO$(1-0)$emission. The ^{13}CO$(1-0)$ emission is much fainter for NGC6764 (we will discuss exactly how much fainter in Section 3.3.3), which causes the ^{13}CO$(1-0)$ results to be more dominated by noise. The emission distribution is also more concentrated in the center, on a scale of only $20''$. Compare to the ^{13}CO map, the ^{13}CO emission is more asymmetric: it only extend to the southwest arm. The velocity field of ^{13}CO indicates the eastern side of the center is redshifted and western is blueshifted, which are consistent with the ^{12}CO results.

The relative shape of the ^{12}CO$(1-0)$ and ^{13}CO$(1-0)$ emission lines can be compared by viewing Figure 2 and 5. The shape of the ^{12}CO$(1-0)$ emission was elliptical with a small extension in the lower right direction (see Figure 2). However, by looking at Figure 5, the ^{13}CO$(1-0)$ emission has a small extension in the top left direction and a large extension in the lower right.

Conclusions on whether the width of the ^{13}CO$(1-0)$ spectra changes with respect to the distance from the center are hard to draw due to low signal-to-noise (see Figure 6). However, we can say that we do see a significant signal and that the width of the spectra is comparable to the width of the ^{12}CO$(1-0)$ spectra. In Section 3.3.3, the ^{12}CO$(1-0)$ and ^{13}CO$(1-0)$ spectra will be compared to calculate the ratio of the emissions.

3.3.3. Line Ratio

By directly comparing the integrated intensity of ^{13}CO$(1-0)$ and ^{12}CO$(1-0)$, we obtained the $\mathcal{R}(^{12}\mathrm{CO}/^{13}\mathrm{CO})$ map of NGC6746. The map of $\mathcal{R}(^{12}\mathrm{CO}/^{13}\mathrm{CO})$ is displayed in Figure 7. We find the line ratio $\mathcal{R}(^{12}\mathrm{CO}/^{13}\mathrm{CO})$ is ~ 20 in the center. The high value of the ratio suggests that there is starburst in the center of the galaxy. The map also shows $\mathcal{R}(^{12}\mathrm{CO}/^{13}\mathrm{CO})$ is decreasing with lager radius in the southwest.

Figure 8 displays the ratio of ^{12}CO/^{13}CO for the five positions in Figure 2. The ratio is fairly consistent across the different positions, with a peak ratio of $\sim$20. However, the ratio does seem to decrease slightly as the position moves away from the center of the object.

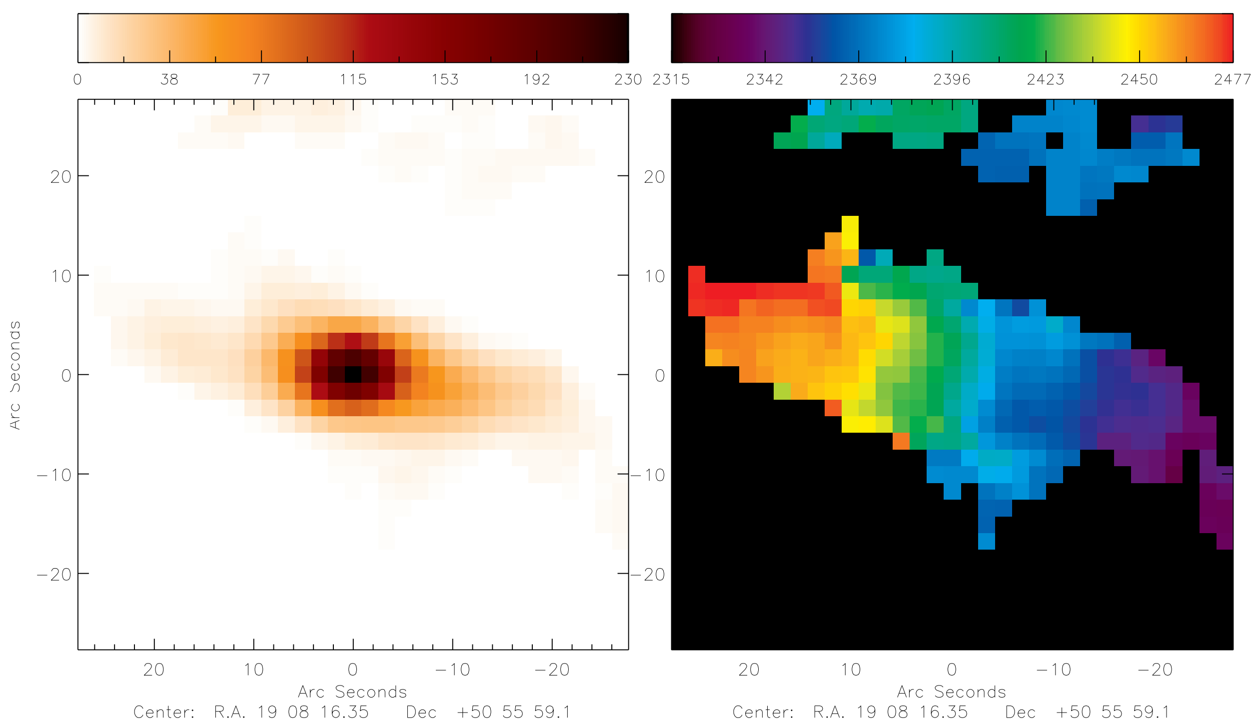

Fig. 1.—: Left: ^{12}CO integrated intensity map of NGC6764. Right: ^{12}CO velocity field.

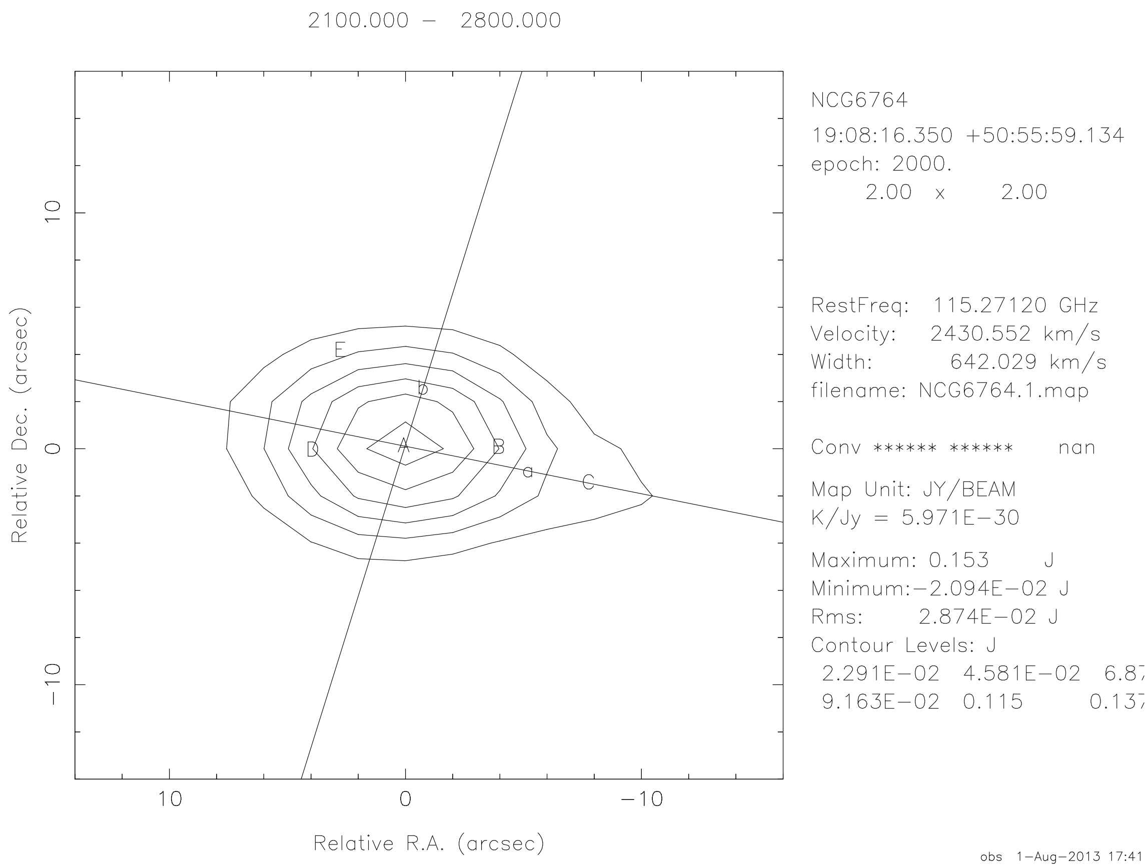

Fig. 2.—: The moment 0 contour map for the ^{12}CO$(1-0)$ emission line is shown with five different positions labeled (A,B,C,D,E). Two intersection lines are also labeled which are not used in this paper. The spectra of each of these positions will be shown in Figure 3.

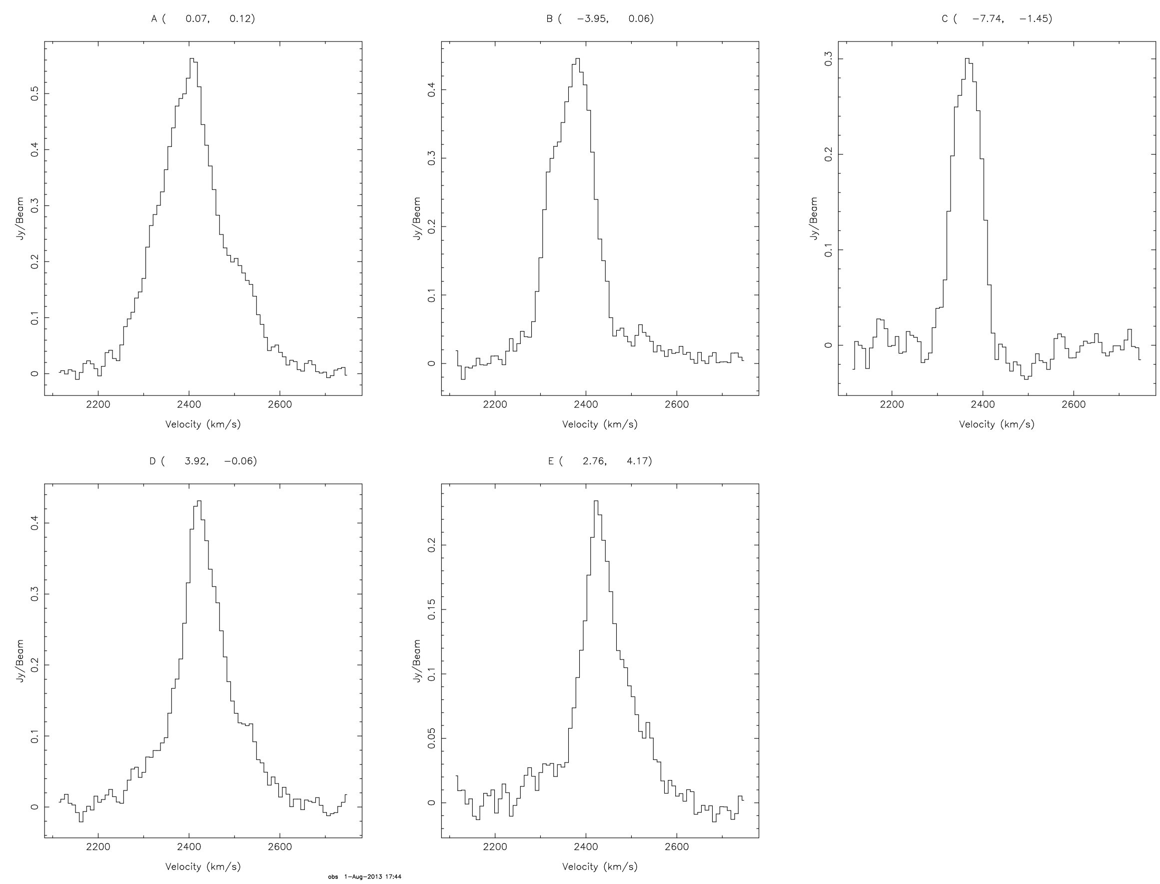

Fig. 3.—: ^{12}CO The spectra for each of the five positions seen in Figure 2 is shown for the ^{12}CO$(1-0)$ emission line. The spectra are Hanning smoothed to reduce noise. The width of the spectra narrows as the position moves away from the center.

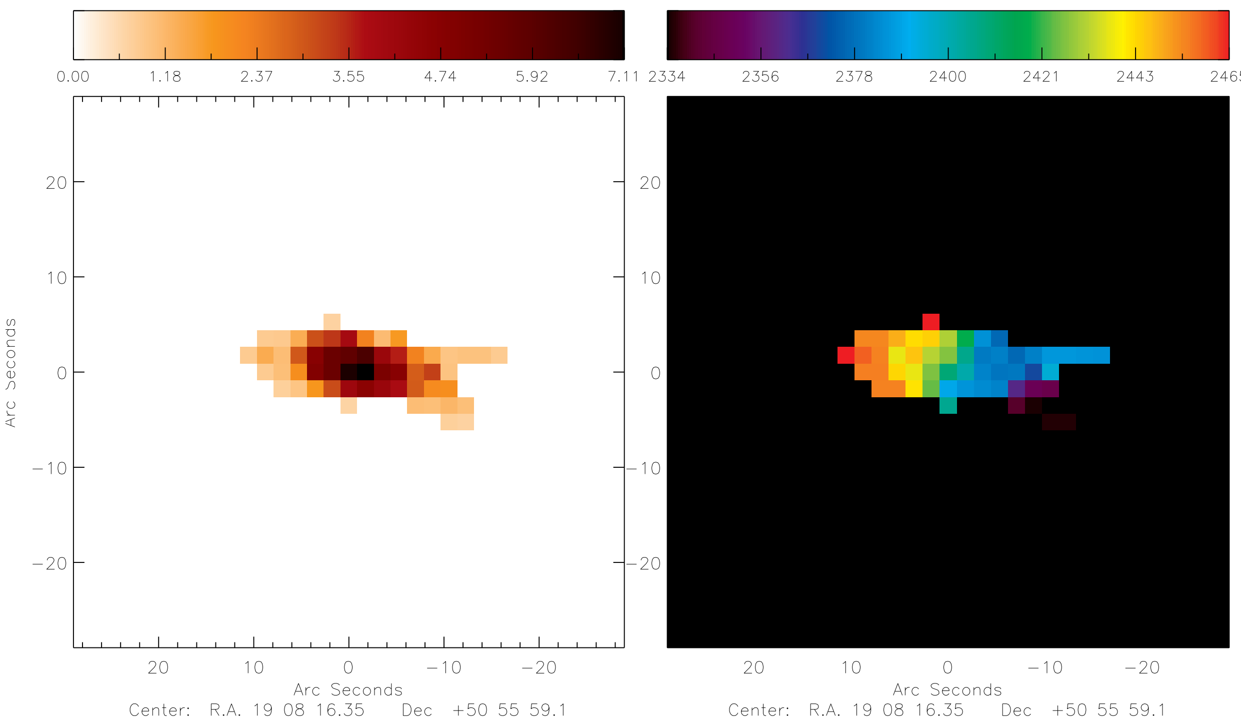

Fig. 4.—: Left: ^{13}CO integrated intensity map. Right: ^{13}CO velocity field.

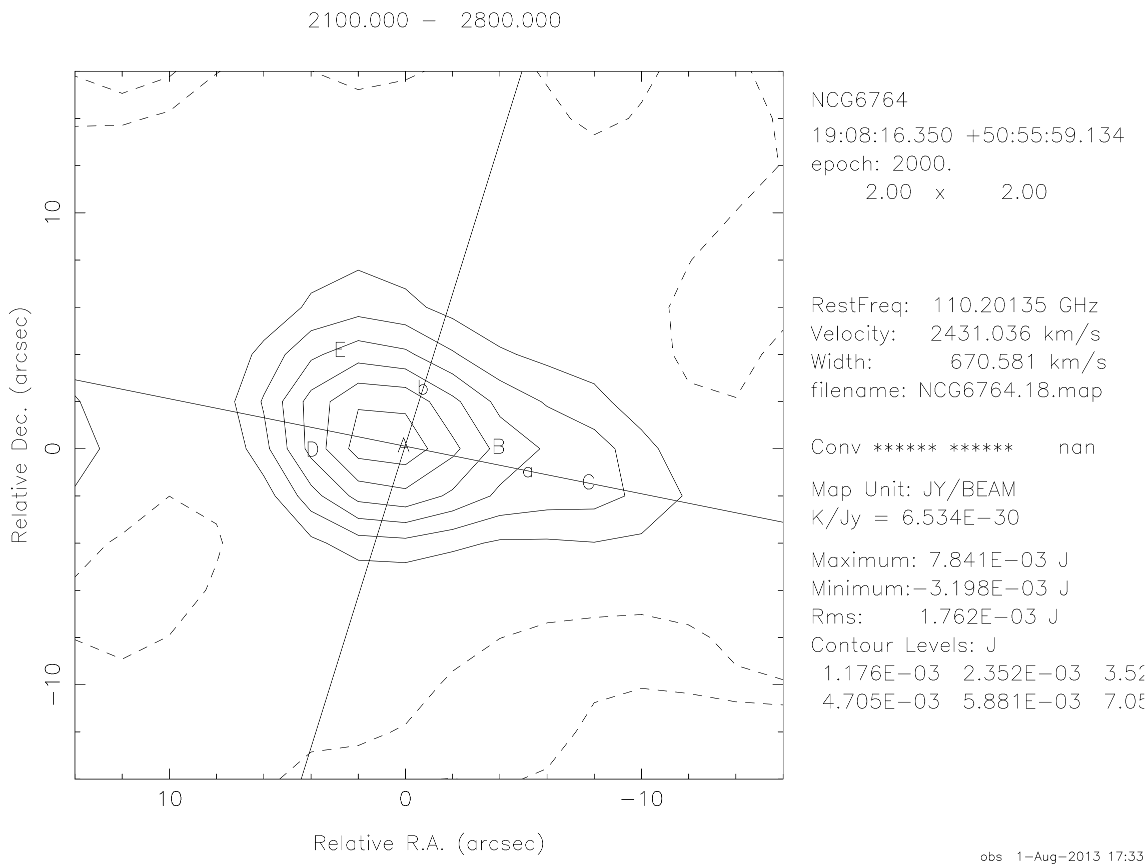

Fig. 5.—: This is the moment 0 contour map for the ^{13}CO$(1-0)$ emission line. The same positions are marked as in Figure 2. The spectra of each position is displayed in Figure 6. The emission line appears to be more spread out than the ^{12}CO$(1-0)$ emission line (see Figure 2 to compare).

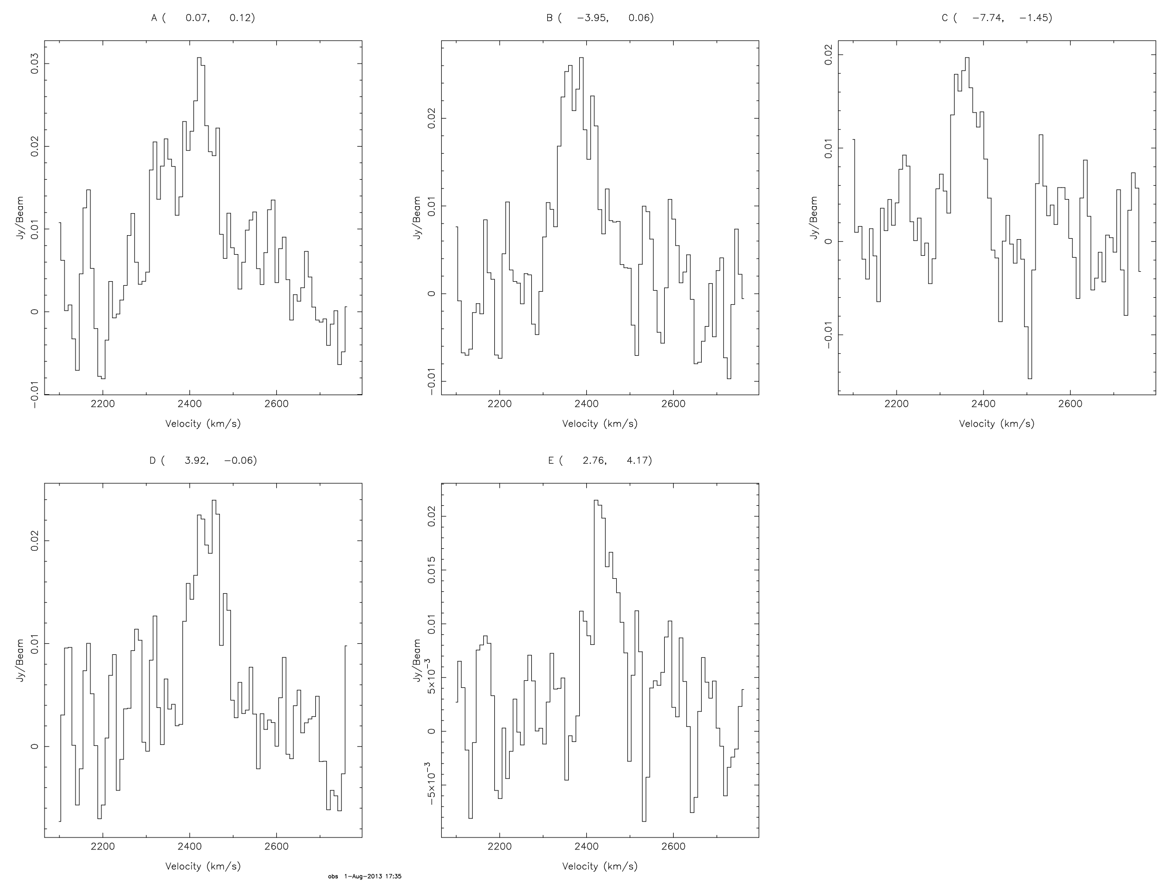

Fig. 6.—: ^{13}CO$(1-0)$ Hanning smoothed spectra has a low signal to noise, making any comment on the width of the spectra impossible. Therefore, the only conclusions are the emission is detected and the width agrees roughly with the spectral width of ^{12}CO$(1-0)$. This spectra is used along with Figure 3 to calculate the emission ratio in Section 3.3.3.

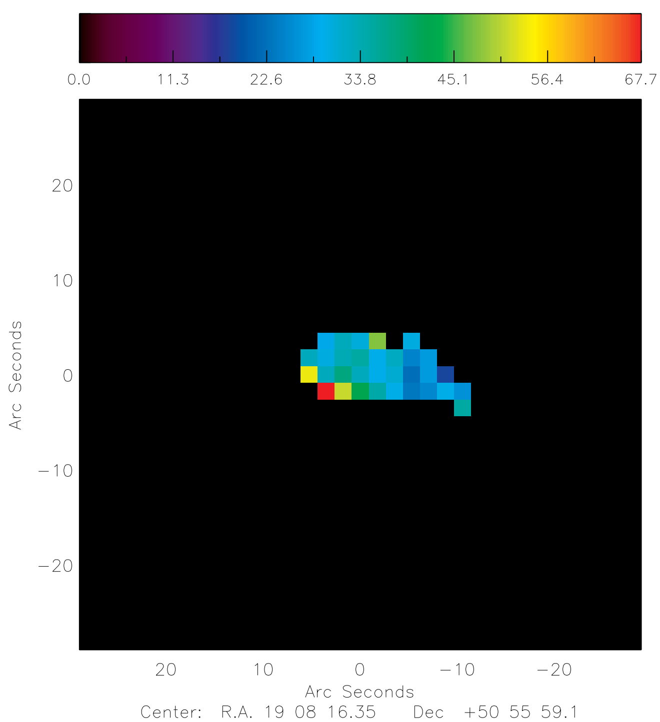

Fig. 7.—: $\mathcal{R}(^{12}CO/^{13}CO)$ map

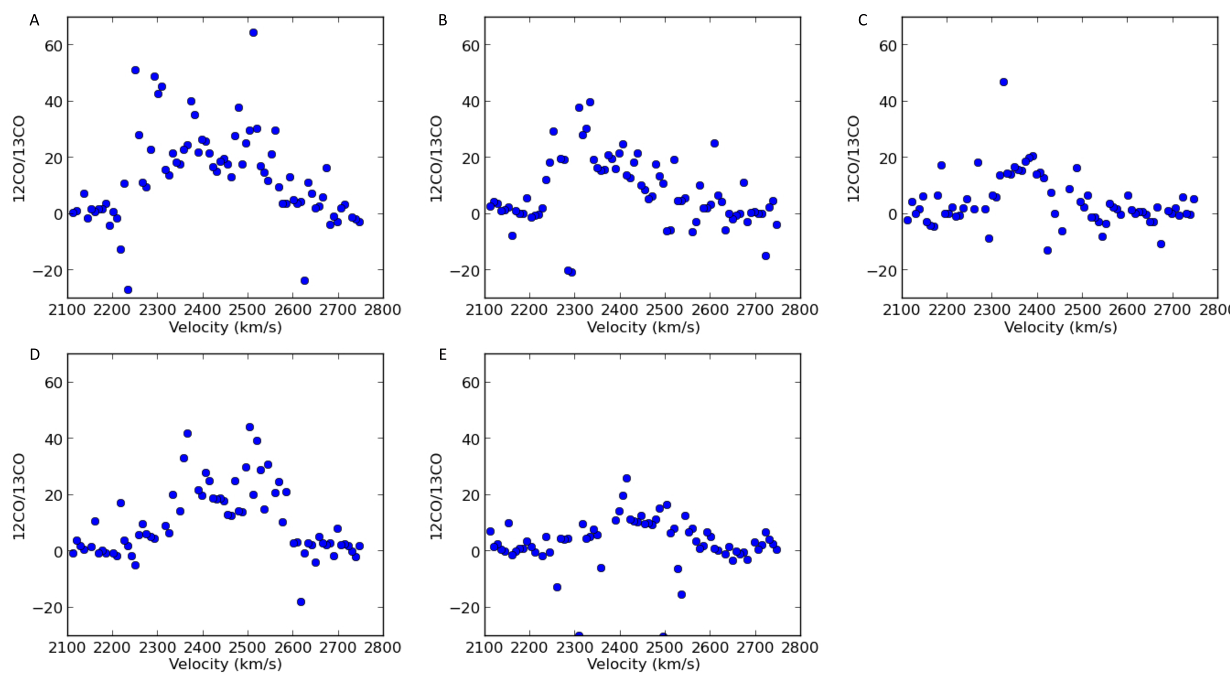

Fig. 8.—: The ratio of ^{12}CO/^{13}CO is shown for each of the five positions originally shown in Figure 2. This was found by dividing the spectra found in Figure 3 point-by-point by the spectra in Figure 6. The ratio at 2400 km/s is around 20.

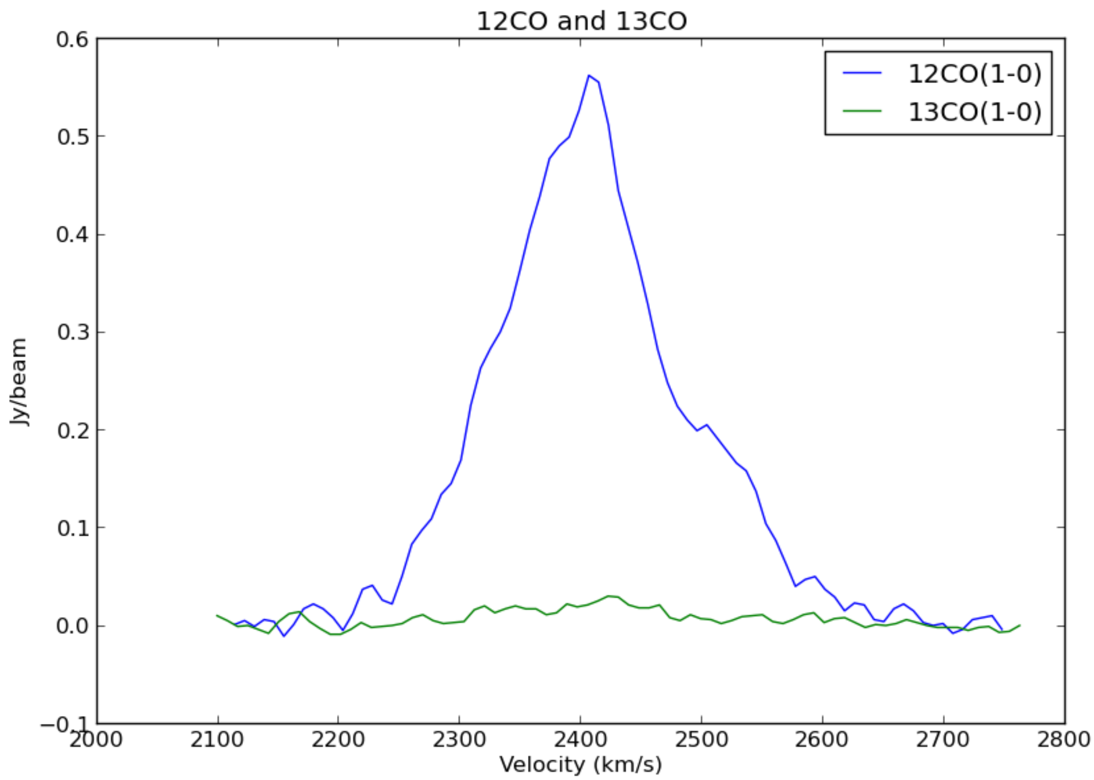

Fig. 9.—: A to-scale plot showing the spectra of the center point of ^{13}CO and ^{12}CO on top of each other. To get a ratio for this, we integrated over the width of the detection for ^{13}CO and ^{12}CO respectively and then calculated a ratio of approximately 19.6 which is consistent with Eckart et al. (1991).

4. Tracing ^{12}CO (1-0) and ^{13}CO (1-0) in Barred Spiral NGC 3627

Melissa Louie, Alfie Tiley, Rosalie McGurk

4.1. Scientific Motivation

To understand the process of star formation in a galaxy it is useful to study its relation to gas dynamics. The dynamics of the gas in spiral galaxies can influence or even trigger star formation Roberts (1969). H_2 is the most abundant molecular gas, but due to the low temperatures H_2 cannot be directly detected. However, the H_2 distribution is well-traced via the emission lines of CO, the most prominent of which fall within millimeter (mm) wavebands. Combined Array for Millimeter-wave Astronomy (CARMA) allows us to observe these mm molecular lines and image the molecular gas in large areas of nearby galaxies. With CARMA we can also observe different isotopes of CO revealing information on the physical conditions of the gas, i.e. density and temperature.

The bulk of recent star formation appears in spiral galaxies. Since they are gas-rich, they are good candidates in which to study the relation between gas dynamics and star formation. Molecular gas is organized in giant molecular clouds (GMCs). These GMCs can act as stellar nurseries, facilitating the formation of stars via gravitational collapse. In light of this, NGC 3627 (at 8.6 Mpc), was chosen as a suitable candidate to pursue this study as it has both a strong central bar and spiral arms. We aimed to study the gas structure and dynamics of ^{12}CO in NGC 3627. We also compared the gas distribution of ^{12}CO to ^{13}CO and recent star formation tracers, 24μm and Hα.

4.2. Observations and Data Reduction

We observed NGC 3627 for a total of ten hours using the Combined Array for Research in Millimeter Astronomy (CARMA) array. The array of 6.1 and 10.4-m antennas was in E configuration, with baselines ranging between 8.5m and 66m. We used a seven-point mosaic to image the central region of NGC 3627. We observed NGC 3627 for 5 hours on both 2013 July 30 and 31; two hours of the total observing time were lost on 2013 July 30 due to poor weather conditions. The passband calibrator was 0854+201 on July 30 and 0927+390 on July 31. Both observations used Mars as the flux calibrator and 1058+015 as the gain calibrator; the gain calibrator was observed for 3 minutes between observations of the full seven point mosaic pattern. Each mosaic pointing is observed for 2.5 minutes during each mosaic cycle.

We observed ^{12}CO (1-0) (115.271 GHz), ^{13} CO (1-0) (110.201 GHz), and C^{18}O (109.782 GHz) with a bandwidth of 125 MHz, 125 MHz, and 250 MHz, respectively. Two narrow bands, overlapping by a few channels, were placed around the ^{12}CO and ^{13}CO lines, to increase the velocity resolution while maintaining full coverage of the line widths. For each of the three spectral lines, we also centered a 500 MHz wide-band on the spectral lines to aid in calibration. We detected both ^{12}CO and ^{13}CO emission but did not detect any C^{18}O emission.

Data was reduced using the package MIRIAD Sault et al. (1995). Images were made using the task *invert* with velocity channel widths of 5 km s^{-1}. The synthesized beams for the ^{12}CO and ^{13}CO are, respectively, 9.3" and 9.0". To create the final maps, the ^{12}CO and ^{13}CO maps were cleaned using the task *mossdi* and convolved with the synthesized beam using *restor*. The channel maps of our measured ^{12}CO are shown in Figure 10. These maps show channels with velocity resolutions of 10 km/s, and sample every fourth channel across our bandwidth.

4.3. Results

4.3.1. ^{12}CO gas distribution

The integrated flux and intensity weighted velocity maps are shown, respectively, in the left and right panels of Figure 11. The CO emission is primarily located in the central, bar, and spiral arm structures. However, we do detect some CO emission in the interarm regions, particularly between the central region and NW spiral arm. We see a buildup of gas at the points where the bar meets the spiral arm structures, typical in barred spirals Kuno et al. (2007). This gas buildup could also be due to an inner ring present in the galaxy Regan et al. (2002). We also see a slight asymmetry in the CO distribution in the spiral arms, which could likely be the result of an interaction or merger with another galaxy in the Leo Triplet. From our intensity weighted velocity maps in Figure 11, we see the rotation of the galaxy, and observe a large velocity gradient across the central region of the galaxy.

We also show a position velocity diagram cut across the center of the galaxy, Figure 12. The cut is taken between the two points where the bar meet the spiral arms on opposite sides of the galaxy center. From our position velocity cut, we separate out three different regions with unique dynamics. In the central region, we see a strong feature spanning 350 km s^{-1} and approximately 15"; this feature also has a very strong gradient in velocity and position, suggesting fast rotation in the nuclear region. The bar region seen to the left and right of this central feature extends in radius to 45" NE and SW of the center. We do observe a velocity gradient across the bar, but it is not as strong as the one seen in the center of the galaxy. Centered at $\pm$60", there is buildup of molecular gas where the bar and spiral arm meet.

4.3.2. Comparison of ^{12}CO with ^{13}CO and SF Tracers

In addition to ^{12}CO, we also detected ^{13}CO. Figure 13 shows the ^{13}CO integrated intensity color map with the ^{12}CO emission plotted on top in white contours. In the nuclear region, both tracers are well-aligned. The peaks in the two tracers are also aligned in the lower spiral arm. Interestingly, this is not the case with the upper spiral arm. The ^{13}CO does appear along the spiral arm, but the peaks in the ^{13}CO do not coincide with peaks in the ^{12}CO emission. This suggests that there

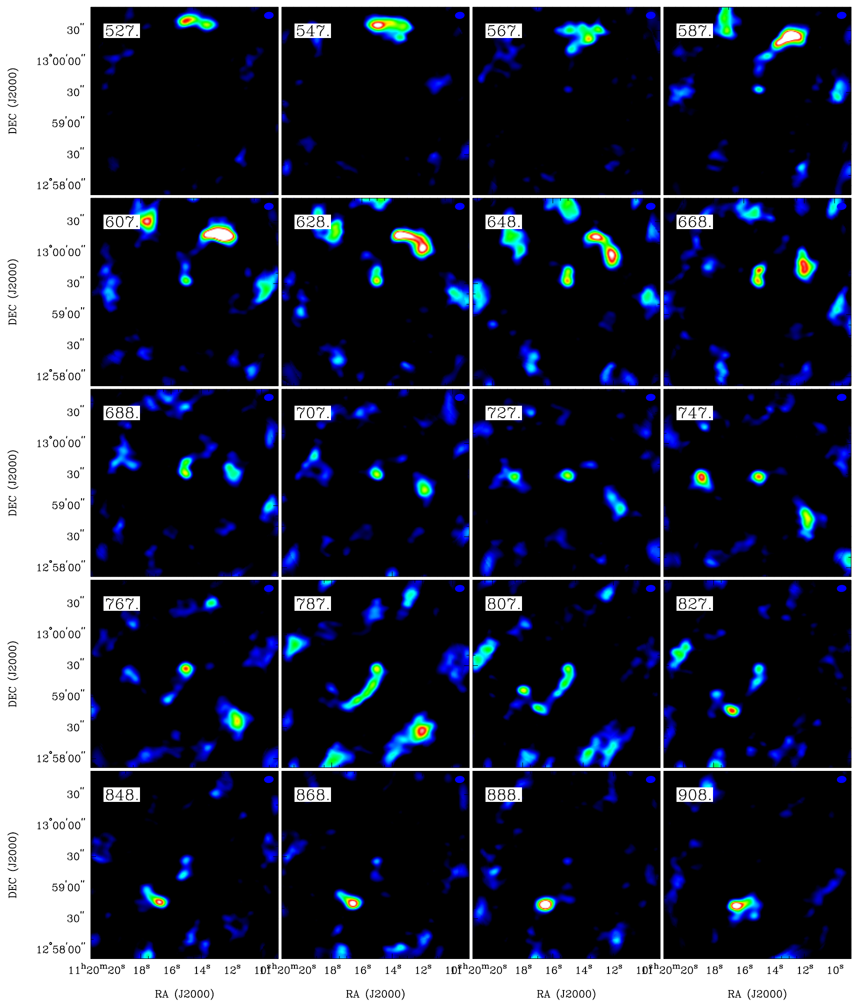

Fig. 10.—: Velocity channels map of NGC 3627. Each channel has a width of 10 km s^{-1} and this figure samples every fourth channel. The beam size is shown in the top right of this image. The kinematic structure of this galaxy is seen changing through the velocity channels.

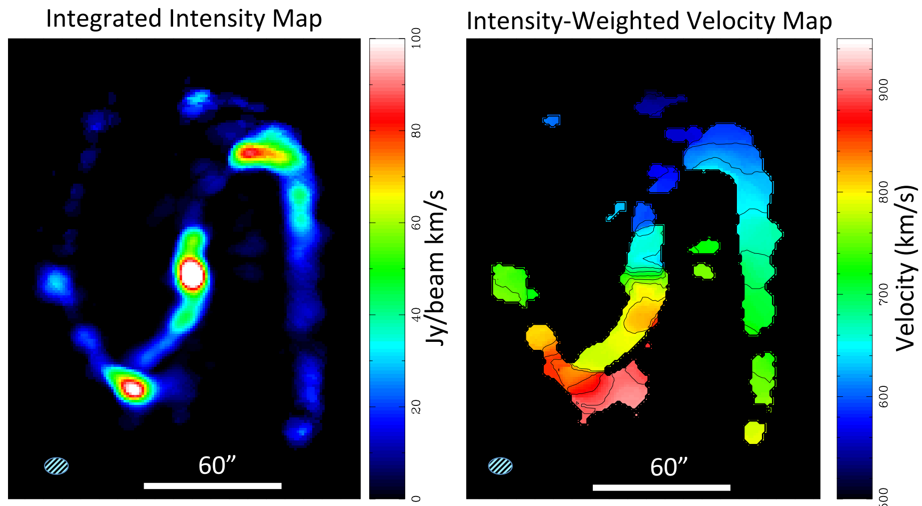

Fig. 11.—: (Left) Integrated intensity map of NGC 3627, in units of Jy beam^{-1} km s^{-1}. Our field of view included the central nucleus, bar and spiral arm regions in NGC 3627. (Right) Intensity weighted velocity map, in units of km s^{-1}. The contours are in steps of 25 km s^{1}. There is a strong velocity gradient across the center of nucleus. For both images the beam size is shown in the bottom left of the image. North is up and east is to the left.

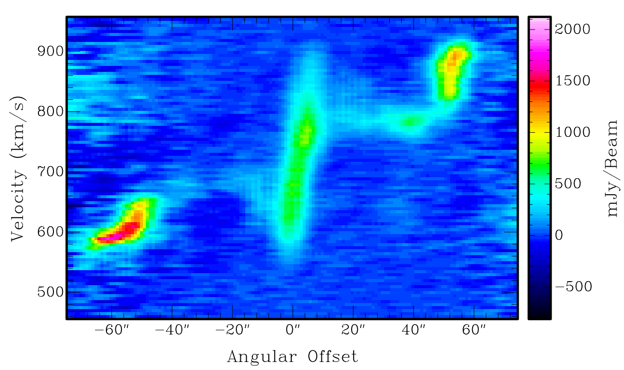

Fig. 12.—: Position-velocity diagram cut taken across the central region of NGC 3627. The velocity cut is taken from the lower left edge of the bar up towards the upper right edge of the bar. The central 15” is the nuclear region, the bar structure is out to ±60” where it meets the spiral arms.

are different physical conditions in the two areas where the bar and spiral arms interact.

If emission from a third molecule was detected, in addition to the ^{13}CO and ^{12}CO, the temperature and density environments in both these peaks could be defined using Large Velocity Gradient analysis Scoville & Solomon (1974). Potential third molecules could include C^{18}O or ^{12}CO(2-1), both observable with CARMA. We searched for C^{18}O emission, but did not detect any during our observations.

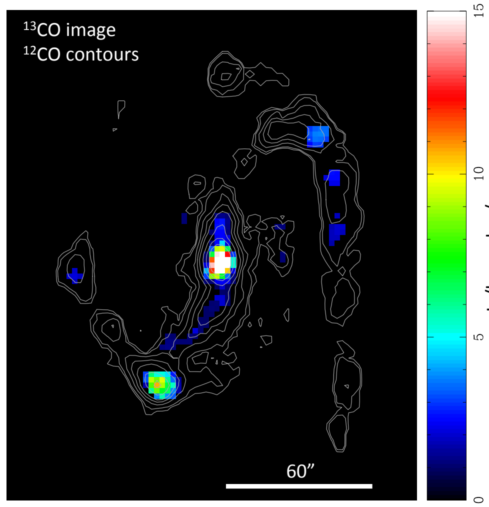

Fig. 13.—: Integrated intensity color map of ^{13}CO with ^{12}CO contours overplotted in white. The ^{13}CO emission is aligned with the ^{12}CO on the lower half of the bar and spiral arm but are not as coincident with the ^{12}CO emission on the upper spiral arm.

We were also interested in comparing the ^{12}CO emission with tracers of recent star formation. In Figure 14 we compare contours of the integrated intensity map of our ^{12}CO emission with the recent star formation tracers 24μm and Hα. These maps are from the Spitzer Nearby Galaxy Survey (SINGS) Kennicutt et al. (2003). The 24μm emission traces warm dust heated by nearby recently formed stars. The Hα emission is directly from newly formed massive stars. The star formation tracers are organized in spiral arm structures. The ^{12}CO emission is aligned with the recent star formation tracers and shows this same spiral arm structure.

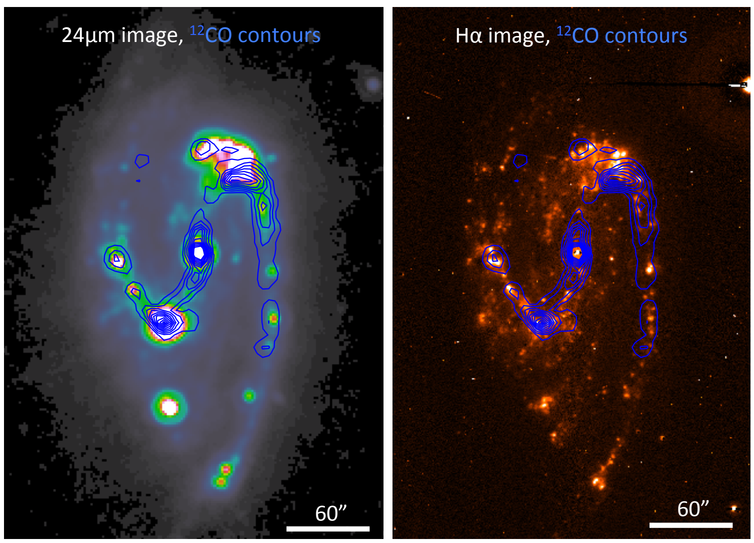

Fig. 14.—: (Left) Spitzer 24 μm emission and (Right) Hα emission from Kennicutt et al. (2003) with our ^{12}CO contours overplotted in blue. Both the 24μm and Hα trace recent star formation. The ^{12}CO is aligned with recent star formation in this galaxy. Both the ^{12}CO and the recent star formation can be traced by the spiral structure.

5. 3mm Observations of Young Stellar Objects
Anna Miotello, Ben Tofflemire, & Emma Yu

5.1. Motivation

The L1551 IRS5 outflow was the first discovered associated with a young stellar object (YSO). We have chosen to observe this system because of its strong line emission and has an angular scale of emission appropriate for the CARMA Array.

UY Aurigae is a circumbinary disk around a young binary system. The primary star has a spectral type of K7 (Herbig et al.1998). It has a companion of spectral type between M0 to M4 (Herbst et al. 1995) at $0''.88$ separation (Close et al. 1998), which corresponds to 130 AU at a distance of 140 pc. The system is known to have strong gas emission, and it was the only binary system detected in ^{13}CO in the Dutrey et al. 1996 survey of 33 young stellar objects in Taurus-Auriga with IRAM. The object has been shown to have a disk under Keplerian rotation, but there hasn't been any detailed study using line shapes to interpret disk properties.

With larger collecting area of CARMA, we may be able to detect ^{13}CO, C^{18}O, and C^{17}O emissions, and probe deeper into the disk interior. The goal of this project is to: 1) learn to observe and reduce the data for both spectral line and continuum observations. 2) try to detect emissions from rare CO isotopologues so that we can probe different layers of the disk.

5.2. Observations & Data Reduction

Observations of L1551 IRS5 and UY Aur utilized the spectral line configuration outlined in Table 1. The remaining three spectral bands were set in 500 MHz continuum windows. A wider spectral region around CN was chosen to ensure adjacent fine-structure lines were included. A single track for L1551 provided 3.3 hours on target. Two shorter tracks of UY Aur totaled 6 hours on target. For both sources, observations of Mars, 3C84, and 0510+180 provided flux, passband, and phase calibration respectively. Observing in the E configuration, our average synthesized beam size was $\sim 7''$ in diameter.

An error in our source catalog did not apply the $\sim$7 km/s LSR shift (Swift et al. 2005) to our observations of L1551. Fortunately, the 20 km/s window of our 8 MHz bands (smallest used) encompassed the velocity range of emission detected in previous works.

Reduction of these data used John Carpenter's *Miriad* shell script provided at the summer school. The script first performs passband response correction to narrow-band spectral windows using a non-astronomical noise source with the *mfcal* task. Second, our astronomical passband calibrator above is applied to the continuum and narrow bands using the *mfcal* and *uvwide* tasks. Flux calibration is then performed using *selfcal* and *bootflux* and finally, gain calibration is applied with *mfcal*. Continuum subtraction was not performed on these data.

5.3. Results

5.3.1. L1551

Figures 15, 16, and 17 display velocity spectra for CO, ^{13}CO, and C^{18}O respectively. We do not detect emission from C^{17}O or CN. CO and ^{13}CO show a double peaked velocity structure indicative of an outflow centered around 6.5 km/s LSR. ^{13}CO in particular reproduces the line profile observed at a lower resolution by Hogerheijde et al. (1998). Our detection of C^{18}O, however, is singly peaked near the system velocity. This agrees with previous C^{18}O observations of L1551 (Hogerheijde et al. 1998) and we conclude that the emission of C^{18}O is originating near the center of the system rather than in the outflow.

A synthesized first moment map (mean velocity) of CO(1-0) is presented in Figure 18. At a distance to L1551 of ∼140 pc, the length of each axis spans 12,000 AU (0.06 pc). In this image the structure of the bipolar outflow is apparent both spatially and kinematically. Some errors may still exist in this preliminary reduction based on the extended, blue-shifted emission in the receding outflow. We observe an outflow opening angle between 90-120°, consistent with values derived from infrared spectroscopy of [Fe II] emission (Pyo et al. 2005).

5.3.2. UY Aur

The data for UY Aur is reduced as described above. Data from Antenna 11 is flagged out due to artificially high system temperature ($> 2000K$) for both segments.

We detected CO, ^{13}CO, and CN in UY Aur. A rotational disk can be seen in the channel map of ^{13}CO (Figure 19), which is consistant with the previous picture of a Keplerian rotational disk with a 43 degree inclination. A significant amount of materials surrounding the disk is detected at the LSR velocity of 6.18 kms^{-1}.

Table 1. Spectral Line Configuration

Line	Rest Frequency (GHz)	Transition	Bandwidth (MHz)
CO	115.271	$J = 1 - 0$	8
CN	113.491	(1-0)	32
C^{17}O	112.359	(1-0)	8
^{13}CO	110.201	(1-0)	8
C^{18}O	109.782	(1-0)	8

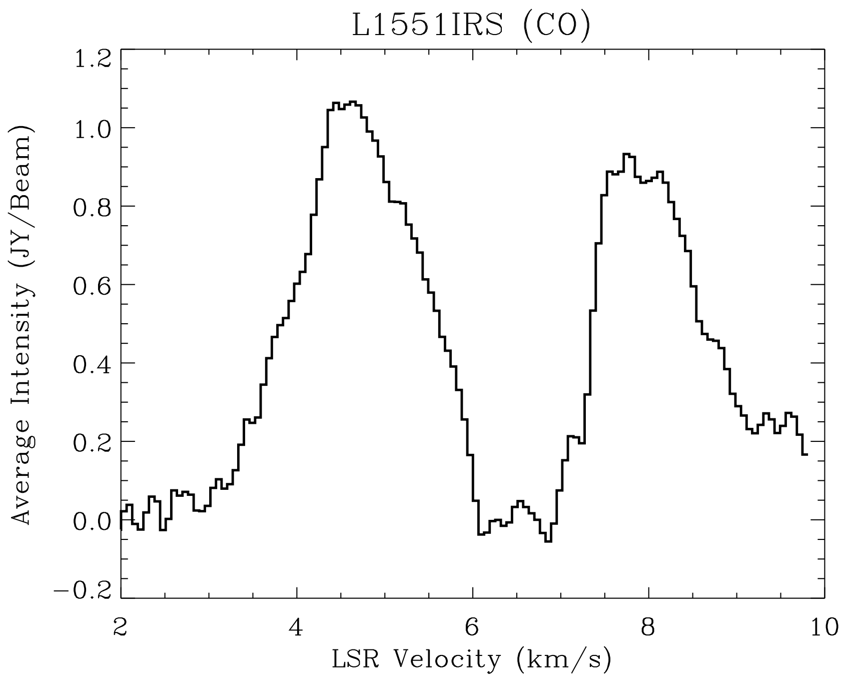

Fig. 15.—: CO velocity spectra of the L1551 outflow. Spectrum is binned by a factor of 3 to reduce noise.

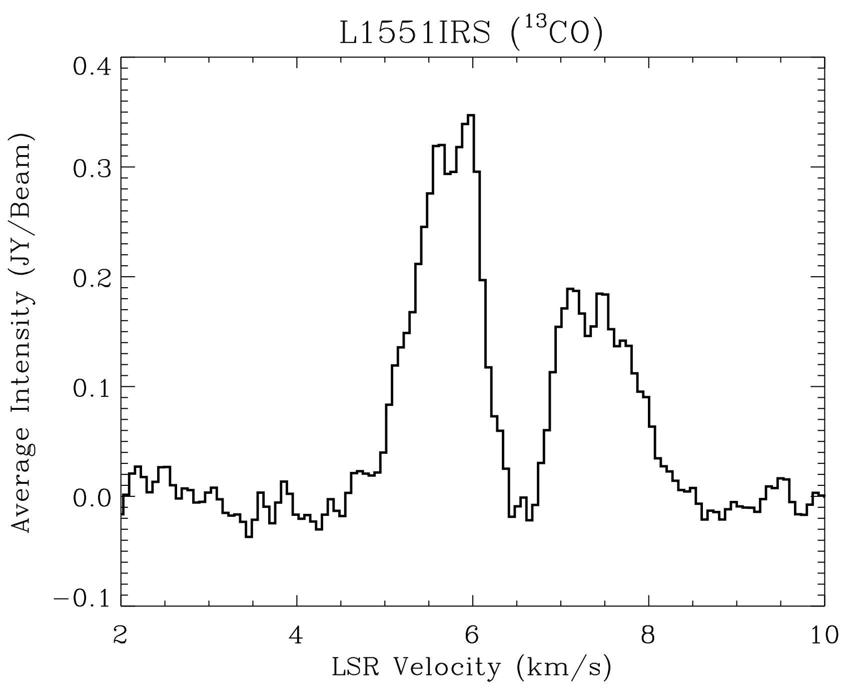

Fig. 16.—: Same as Figure 15 for ^{13}CO.

The spectra of CO and ^{13}CO(1-0) are shown in Figure 20 and Figure 21. We have detection up to 1.5 kms^{-1} off the velocity center, which corresponds to a distance of 400 AU from the central star. The absorption at the velocity center may be contributed by the surrounding envelope seen in the channel map. We may need single dish data to correct for this effect.

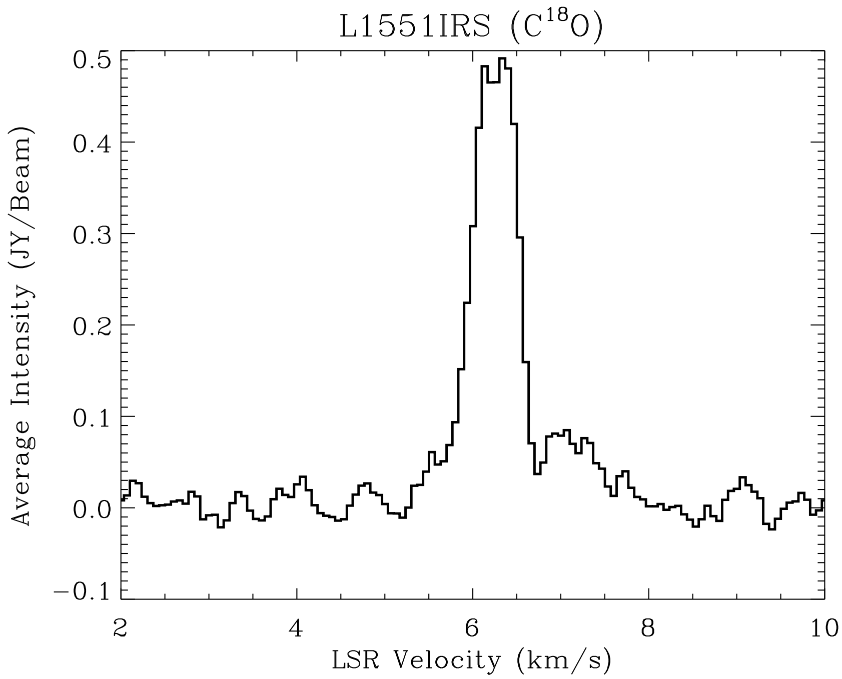

Fig. 17.—: Same as Figure 15 but for $C^{18}O$.

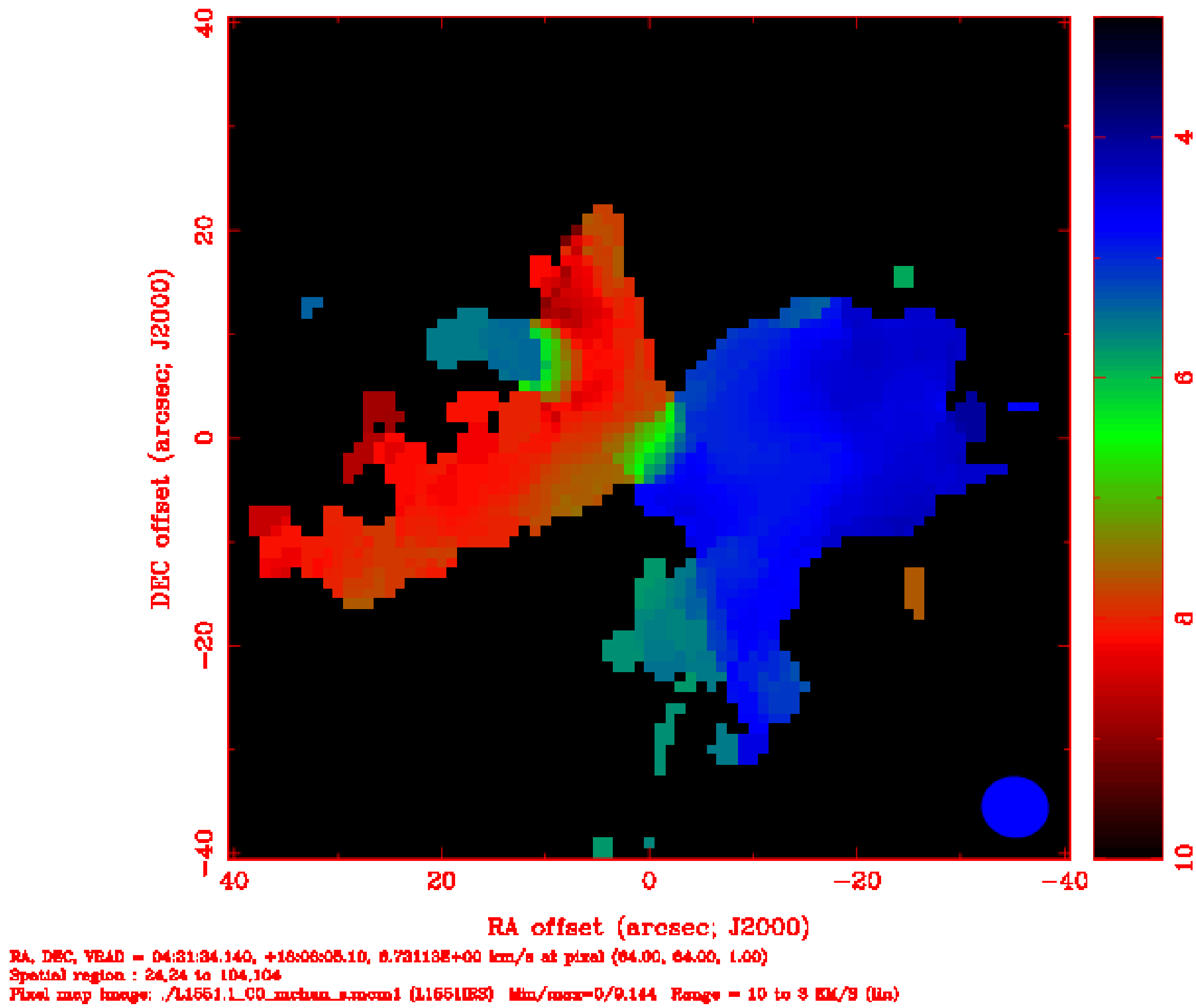

Fig. 18.—: Mean velocity (first moment) map of the L1551 outflow. At a distance of ∼140 pc the x,y scale of this image is 12,000 AU per side.

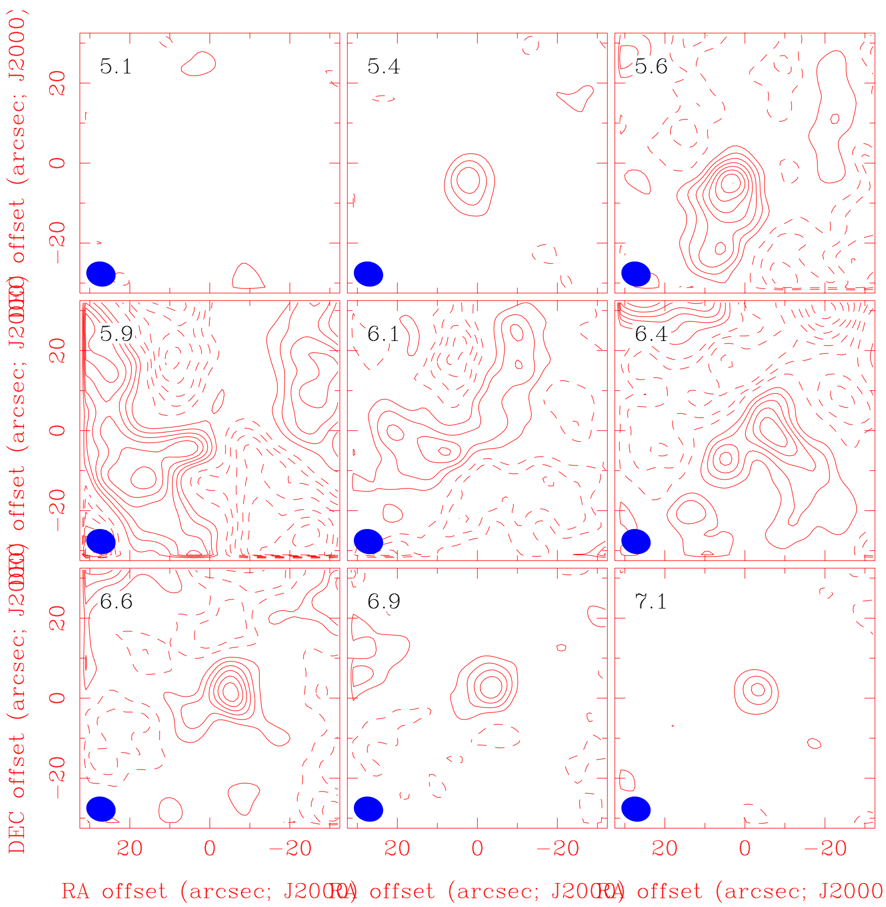

Fig. 19.—: The channel map of ^{13}CO(1-0) line. The LSR velocity of the source is 6.18 km s^{-1}

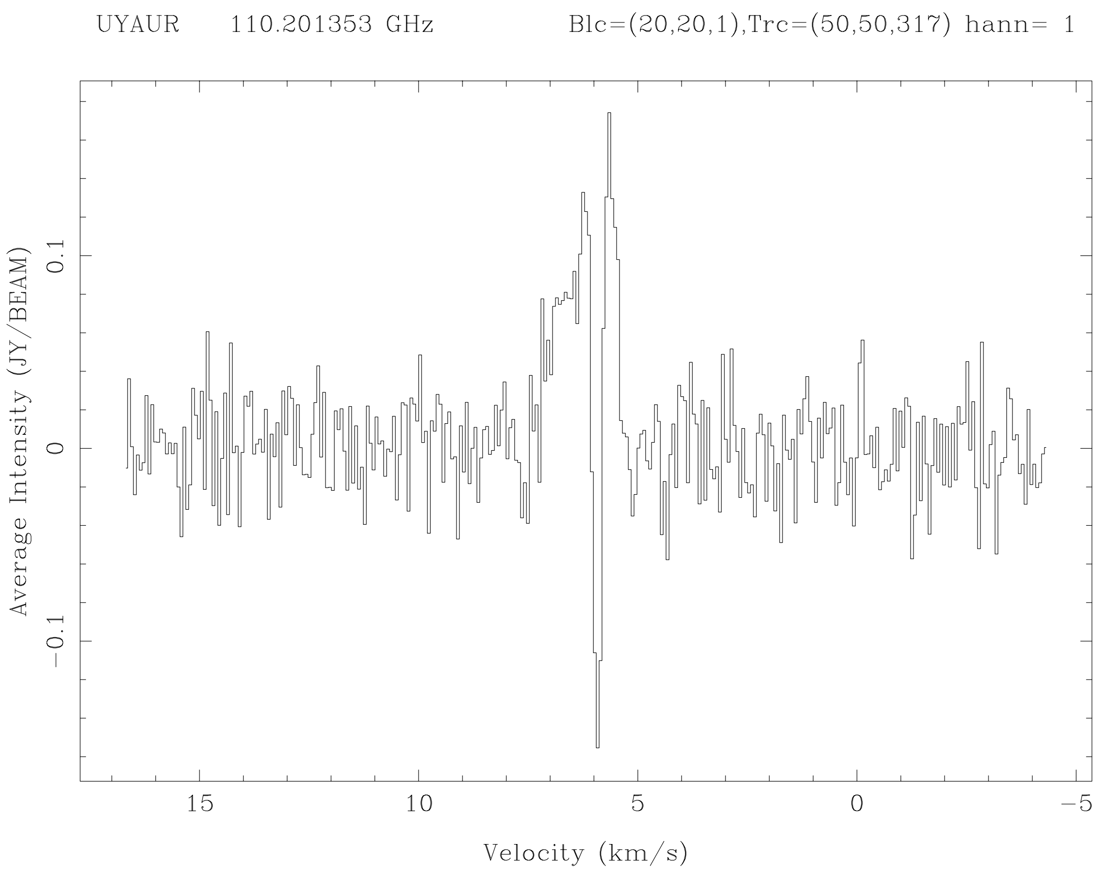

Fig. 20.—: The spectrum of ^{13}CO(1-0) line

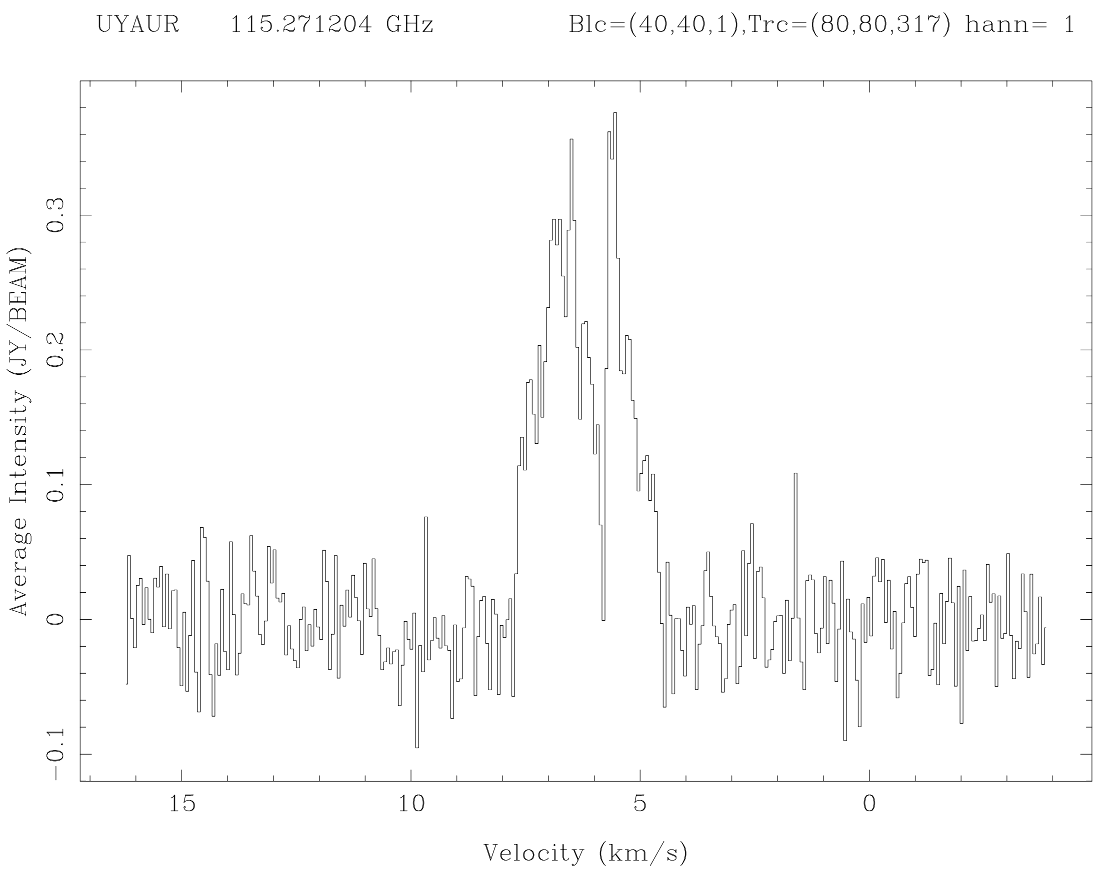

Fig. 21.—: ^{13}CO spectrum

6. Sunyaev-Zel'dovich imaging of MACS J0715.5+3745
Nina Van der Pyl

6.1. Introduction

6.1.1. Galaxy clusters in a nutshell

Galaxy clusters are the largest gravitationally bound objects of the Universe, with mass ranging from 10^{13} to over $10^{15} M_\odot$. Because of their colossal mass their matter content is thought to represent that of the Universe as a whole, making them powerful cosmological probes. In particular, the ratio of baryonic cluster mass M_b (gas + stars + galaxies) to total cluster mass $M_{\rm tot}$ (M_b + dark matter) can be used to measure the cosmic abundance of these components. Thus,

$$f = \frac{M_b}{M_{\rm tot}} = \frac{\Omega_b}{\Omega_M}\,, \qquad (1)$$

where Ω_b and Ω_M are the baryonic and matter density parameters. This so-called baryon fraction test has been widely used in cosmological cluster studies (see *e.g.* LaRoque et al. 2006, which combined X-ray and radio observations).

The key ingredient in any cluster cosmological study is the total cluster mass, which may be estimated in many different ways depending on the wavelength of the observation. For instance, optical masses may be inferred from the caustic method which uses the velocity dispersion of individual member galaxies (see *e.g.* Andreon & Hurn 2010) whereas weak lensing masses are derived from the distortion produced by the dark matter distribution of the cluster on foreground objects. On the other hand, X-ray and radio measurements of cluster mass rely on temperature, density or pressure profiles of the hot intracluster medium (ICM) which can then be related to total mass through the assumption of hydrostatic equilibrium.

6.1.2. The Sunyaev-Zel'dovich effect

Clusters may be studied at different wavelengths, ranging from the radio band up to X-ray wavelengths, passing by the optical. In the radio, clusters are observed at millimeter or centimeter wavelengths through the Sunyaev-Zel'dovich effect (SZE) which is the signal produced by cosmic microwave background (CMB) photons being inversely Compton scattered off hot ICM electrons. The SZ signature is either an increment or decrement with respect to the rest temperature of the CMB, according to the frequency of the experiment (see Fig. 22).

The SZ effect (strictly speacking the thermal SZE) is characterised by the following equation:

$$\Delta T_{\rm CMB} = f(x, T_e)\, T_{\rm CMB} \int \sigma_T\, n_e\, \frac{k_B T_e}{m_e c^2}\, {\rm d}l\,, \qquad (2)$$

where $T_{\rm CMB} = 2.728$K is the CMB temperature , $f(x, T_e)$ describes the frequency dependence of the SZE ($x = h\nu/k_B T_e$), σ_T is the Thomson cross-section and k_B is the Boltzmann constant. Finally,

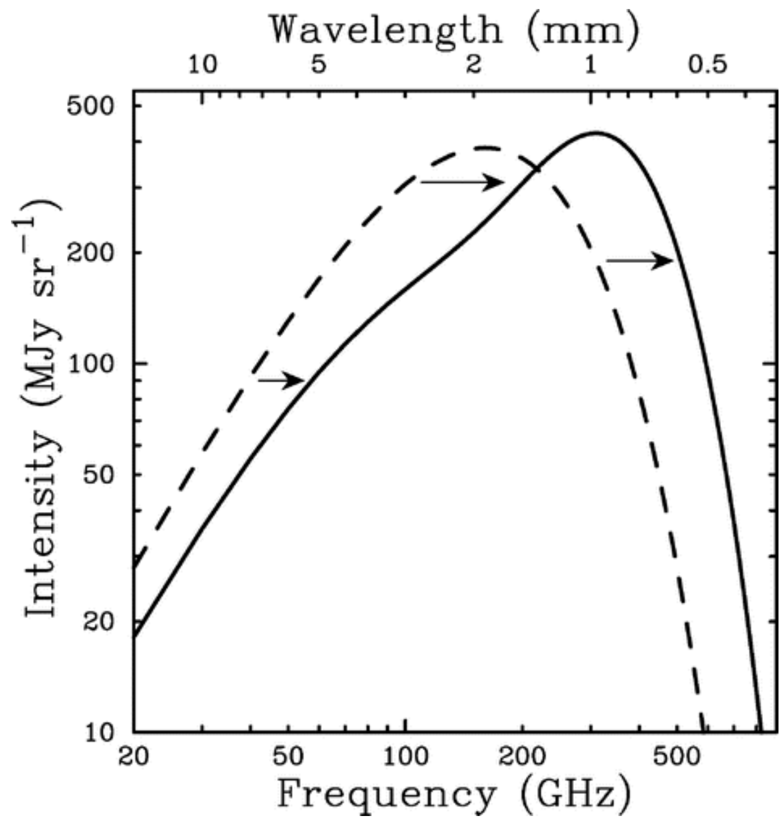

Fig. 22.—: Illustration of the SZ effect. *Dashed curve* - CMB intensity as a function of frequency. *Solid curve* - Distortion in the CMB intensity as a result of the SZ effect. Adapted from Carlstrom et al. (2002).

T_e, n_e and $m_e c^2$ are the electron temperature, density and rest energy, respectively. Note that the integral is along the line of sight dl.

From eq. 2 and using the ideal gas law $P_e = n_e k_B T_e$, it follows that the SZE is proportional to the integrated pressure profile.

6.2. Observations & Motivation

For this project, the intermediate redshift ($z = 0.5458$) cluster MACS J0717.5+3745 (MACS J0717 hereafter) was observed on two consecutive days (Wednesday and Thursday) for a total of $\sim 10\,$hrs using the 3.5 m *SZA* antennas at 30 GHz (1 cm receivers) in the SL configuration.

This cluster has been extensively studied in the X-ray using *Chandra*, the optical and in the radio both at low (Edge et al. 2003; van Weeren et al. 2009) and high frequency using for instance the *SZA* subarray at *CARMA*, *Mustang* or *Bolocam* which operate at 31, 90 and 140 or 268 GHz respectively (see e.g. Ebeling et al. 2004; Mroczkowski et al. 2012). MACS J0717 was first detected in the MAssive Cluster Survey (Ebeling et al. 2001, 2007) and shown to be a rare example of a triple-merging system comprising four distinct groups of galaxies (see Ma et al. 2009, 2008) .

6.3. Data reduction & Imaging

The reduction script provided by John Carpenter was used to reduce the two observation datasets separately. Then, these were combined for the imaging analysis. During the calibration, each calibrator (see Table 2 for a summary of the calibration sources properties) was examined thoroughly and bad data were flagged accordingly. However, since the weather conditions were good at the time of the observations, no major flagging was applied.

Table 2:: Summary of the calibration sources used for the MACS J0717 observation.

Passband calibration		Gain calibration		Flux calibration	
Name	Interval [minutes]	Name	Interval [minutes]	Name	Interval [minutes]
3C84	5.0	0646+448	25.0	Mars	1.0

The accepted visibilities from the two datasets were then combined for imaging. First, the antenna beam pattern (*a.k.a. "dirty map"*; see Fig. 23a) and synthesized beam (see Fig. 23b) were created with the *Miriad* INVERT subroutine using uniform weighting. In order to smooth-out the maps, a 250" FWHM Gaussian filter was applied. Since the inclusion of the outrigger antennas did not change the shape of the maps; in the following imaging analysis, all antennas were used.

Next, deconvolution was performed using the CLEAN algorithm, afterwhich the source model was reconvolved with a Gaussian fit to the central lobe of the synthesized beam. The so-called "clean"-ed map produced for MACS J0717 is shown in Fig. 24.

6.4. Results

The map shown in Fig. 24 shows the SZ effect detected by *CARMA* in MACS J0717. The peak of the SZ decrement is located at $\alpha = 07:17:30.00$; $\delta = +37:45:35.00$ (J2000) and has a value of $-464\,\mu$Jy ($\sim 5\sigma$).

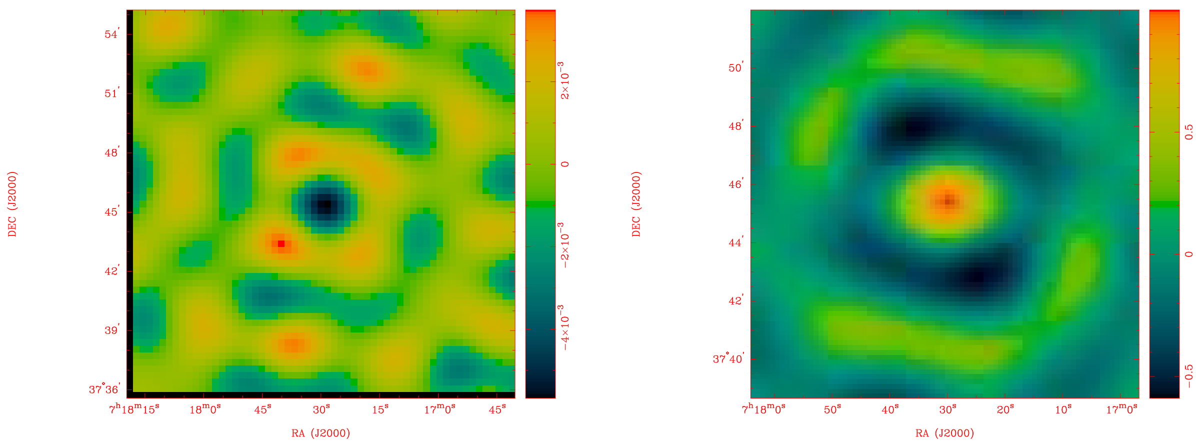

(a) Antenna beam pattern

(b) Synthesized beam

Fig. 23.—: Maps of the antenna beam pattern and of the synthesized beam created with the CLEAN subroutine using a 250" FWHM Gaussian filter and uniform weighting on the data.

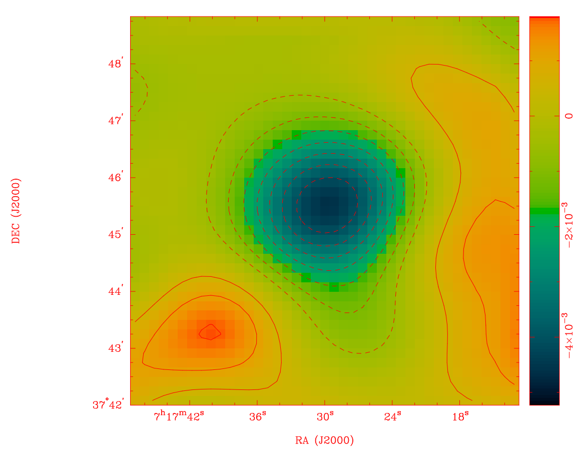

Fig. 24.—: "Clean" map showing the SZ effect for MACS J0717. The contours in the image are set at 10% of the peak intensity. Note that dashed lines represent negative values whereas solid lines are positive.

7. Modeling of Saturn as a CMB polarization calibrator

Moumita Aich (UKZN, Durban)

7.1. Introduction and Motivation

High precision CMB polarization experiments are the current frontiers of cosmology, aiming to improve our understanding about the early universe and large scale structure formation. Experiments aimed at making high-precision measurements of the CMB anisotropy require accurate knowledge of the angular response of the instrument and absolute calibration to a few percent level accuracy or better. For experiments targeting the CMB polarization signal, the polarization fraction and polarization orientation must also be measured to high accuracy. ACTPol, a ground based CMB polarization experiment is one such experiment which will target to constrain parameters e.g., the sum of the neutrino masses through measurement of the weaker polarization B-modes sourced by gravitational lensing. This relies critically on an accurate calibration of the polarization angle as miscalibration mixes the two modes of polarization, the stronger E-modes into the weaker B-modes.

For the case of ACTPol which has arc-minute resolution, a bright and well-measured compact polarized source is necessary for polarization calibration. It is particularly challenging as there are a dearth of non-variable, and compact polarized celestial sources bright at mm-wavelengths. We aim to observe Saturn in polarization at mm wavelengths. Saturn is bright enough to be detected as a microwave source Weiland & et al. (2011). Its brightness and relatively high degree of polarization that arises from scattering of Saturnian light - Grossman et al. (1989) makes it suitable as a polarization calibrator. However, the polarization fraction will change, and angle may change as Saturn moves about the sky. Therefore, we wish to image Saturn's polarized light so we can develop a model for Saturn as a polarization calibrator. If successful, we anticipate using Saturn as the primary polarization calibrator for ACTpol.

We had observed Saturn during August, 2012 and obtained some results for the polarization pattern. We do a similar observation during the summer school in 2013 to verify some of the previous results and check more precisely for instrumental polarization leakages.

7.2. Observations & Data Reduction

Since polarization is unavailable at 3mm, we have used CARMA 1mm E-array configuration (using the 10m and 6m antennae) to observe Saturn at (α, δ) = (14:14:25.41, -10:58:50.48). The quasar 3C279 at (α, δ) = (12:56:11.17,-5:47:21.52) with a flux of 12.4 Jy at 220 GHz, was close and bright enough to be used as our phase and gain calibrator. We used a three point mosaic for Saturn, one at the center and two on either side of the ring. Ideally we need to have offset pointings for the calibrator too which would help in the final data analysis to correct for the instrumental polarization. Due to complications involved and limited observing time, we avoided this during this time slot. (However we include figures of the polarization contours overlayed with the intensity maps for two of the twelve calibrator offsets used in our previous analysis.) The weather was sub-optimal, with a total opacity $\tau = 1.40$. We got a E-array score of 78, which was considered grade C+. The total observation time was 3.54 hours.

We used Miriad for the data analysis. After flagging a couple of bad data points and applying baseline solution, we derive XY phase (the LCP-RCP phase difference) calibration solutions for the polarization data using *xyauto* command of Miriad. After the passband correction and leakage calibration, we generate maps from the fully calibrated data using *invert* task with *mosaic* options. For the deconvolution process, instead of using the standard *clean* algorithm, we have used *mossdi* deconvolution algorithm which is usually utilized for extended sources. We perform iterative phase-only *selfcal* on Saturn. However, instead of using a model for Saturn during *selfcal*, we use *apriori* option which does not assume any model for the source. Using these new calibration solutions, we generate the final maps of the source for both intensity and polarization.

7.3. Results

The map on the left panel of Fig. 25 shows the total intensity maps of Saturn with polarization vectors. It is interesting to note that there is 1.5% fractional polarization on the disk of Saturn. However, the puzzling feature we saw was the asymmetric 10% fractional polarization only on the west side of the rings of Saturn. The map on the right panel of Fig. 25 shows the polarization contours for Q (in red) and U (in blue) on gray-scale intensity map. The solid contours are for positive Q/U while the dashed contours represent negative Q/U. This also clearly shows that there is high polarization asymmetric on the east and west side of the rings.

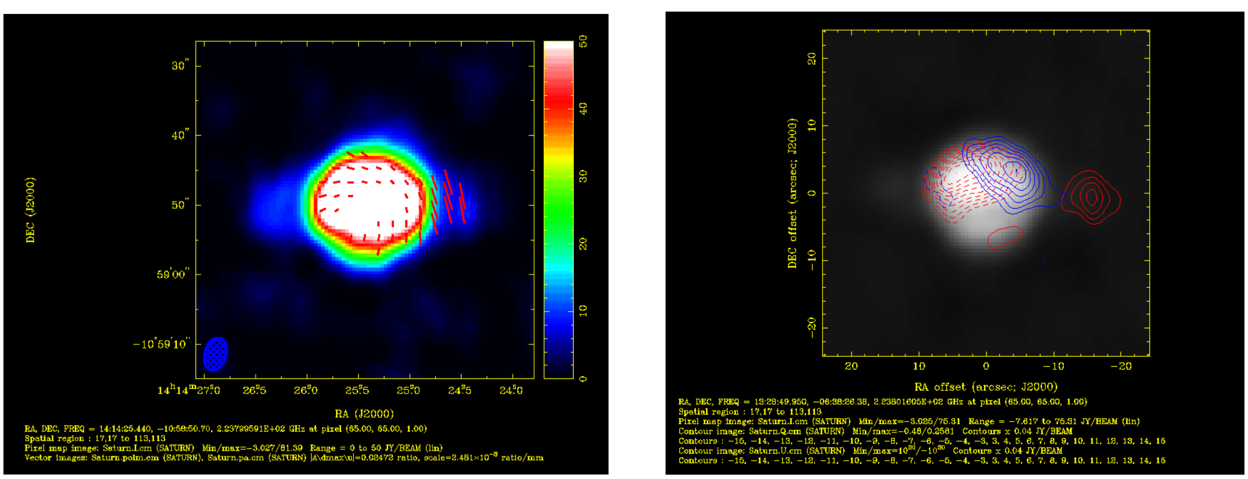

Fig. 25.—: *Left*: Saturn intensity map overlayed with polarization vectors. *Right*: Saturn polarization Q (red) and U (blue) contours overlayed on gray-scale intensity map of Saturn.

We did some checks with some example scripts in Miriad ($MIR/demo/carma/stokes.csh) where we check the effect of a small fractional instrumental polarization leakage due to a Gaussian beam at the center. The FWHM of the beam is manually adjusted to match Saturn's polarization intensity obtained during the data analysis. It is seen that a 1% leakage could give rise to the Q/U contour patterns obtained as shown in Fig. 25.

Using the calibrator offsets, we could in principle model the instrumental polarization and use it correct the obtained polarization pattern of Saturn. However, there are complications involved as a simple weighted average would not be sufficient to cancel out the strong asymmetric polarization pattern as seen in Fig. 25. We had done a complete analysis previously with twelve offsets for the calibrator. In Fig. 26 we show the maps for the calibrator and two of its offsets.

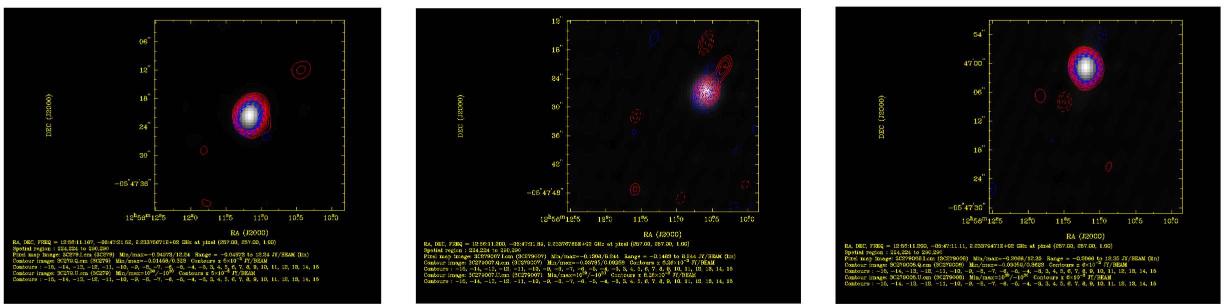

Fig. 26.—: Polarization contours Q (red) and U (blue) overlayed on gray-scale intensity map for the calibrator 3C279 and two of its offsets.

There are other complications involved. We have used only the central pointing of Saturn during *selfcal* and *invert*. Thus the complete n-point mosaic information is lost during the final stages. We tried to extract the information using the Miriad task *demos*, which performs an inverse mosaicing operation for various pointings of Saturn for the three various antenna configurations in the the E-array (OVRO, CARMA and their cross-correlations). Performing *selfcal* on each pointings, we find the gain solutions do not match for the sets of antennae. In principle it is possible to only choose the OVRO (or the CARMA) antennae, for which the gain solutions would match for each pointing; however that would reduce the signal-to-noise ratio by a considerable factor.

7.4. Discussion

We have observed Saturn in polarization twice separated by a period of 10 months. Apart from the the difference in SNR, there is no change in the pattern of the polarization in both the observations. We have checked that the asymmetric polarization pattern we see on Saturn's rings, could be a contributed by the instrumental polarization leakage. However, the 10% fractional polarization signal on the west side of the ring is higher than expected from only instrumental polarization leakage. A possible explanation could be that this asymmetry actually rises from some physical phenomenon. It is know that in parts of the A and B rings the particles are organized into elongated aggregates known as self-gravity wakes Colwell & et al. (2007). Self-gravitating wakes could tend to give a polarization. The wakes tend to be in the A ring and trail rotation by about 22 degrees. Light, coming from Saturn would be more likely to bounce of the West side wakes and perhaps pick up more polarization than the East side wakes, since light would have to transmit through the wakes more. Future work will involve a more detailed analysis of the data, involving greater analysis of the mosaics of Saturn and offsets of the calibrator to check for instrumental polarization.

Acknowledgment

The CARMA summer school 2013 was a great opportunity to learn the intricacies of radio data analysis from experts in the field. All the comments and directions were very constructive to understand our observations. Thanks to all instructors and organizers of the school and fellow participants.

8. Tracing Massive Star Formation in Massive Starless Core in IRDC
Shuo Kong

The initial conditions are critical for understanding massive star formation (MSF). Unlike low-mass star formation, MSF evolves very quickly. During the early stage, the proto-star is still deeply embedded in molecular cloud with high extinction, which makes it hard for us to know how massive star forms. Therefore, instead of trying to directly study its formation activity, it could be useful to investigate the initial conditions. This is the observational motivation. In theory, two models have been proposed to describe the massive star formation. In Turbulent Core Accretion models, molecular gas is first organized into massive, self-gravitating starless, pre-stellar cores (PSCs) that are scaled-up versions of those known to form low-mass stars (McKee & Tan 2003). Alternatively, in Competitive Accretion models, the gas supply to the massive protostar is dominated by Bondi-Hoyle accretion of previously unbound gas (Bonnell et al. 2001; Wang et al. 2010). Since these models involve very different initial conditions, we can distinguish between them by searching for and characterizing massive PSCs. This is the theoretical motivation for observing massive cores.

Infrared Dark Clouds (IRDCs) are particularly dense and cold parts of molecular clouds - they are likely to be the sites of future massive star formation (Rathborne et al. 2006; Butler & Tan 2009, 2012), and thus good locations to search for massive PSCs. In our previous work (Butler & Tan 2009, 2012), we have identified a sample of about 40 candidate massive PSCs from 8 μm extinction maps. From this sample, we picked four cores, C1, F1, F2, G2, which are also dark at 24 μm (Spitzer-MIPS) and 70 μm (Herschel-PACS). We studied their level of deuteration of N_2H^+ with the IRAM 30m telescope ($\sim 16''$ resolution), finding spectacularly high values of $f_D \equiv [N_2D^+]/[N_2H^+] \sim 0.5$ (Fontani et al. 2011). High levels of deuteration are indicators of cold ($T \sim 10$ K), dense gas, with high depletion factors of molecules like CO into dust grain ice mantles (Dalgarno & Lepp 1984), giving further evidence that these massive cores are starless.

We followed-up with $2''$ ALMA Cycle 0 (Tan et al. 2013), identifying about 8 cores that are several arcseconds in size in N_2D^+ and DCO^+. Now with CARMA I want to detect the undeuterated species, N_2H^+ and HCO^+, then we can constrain detailed chemical models of the deuteration process on the angular scale of the cores, which will tell us their chemical ages.

I used CARMA 15-element array (Sci1) to observe G2 at 3 mm wavelength. I used single-polarization and single pointing toward G2. I used the "3 mm High Density Lines" preset in CGS tool. This set-up contains NH_2D, SiO, HCN, HCO^+, N_2H^+, CS. The line width appears to be very narrow ~ 0.5 km s^{-1} in our previous observations, so I choose narrow band with a velocity resolution ≈ 0.08 km s^{-1}. The resulting beam size is about 9" which is comparable to our core size based on N_2D^+ observation.

The observation progressed well except that I lost antenna 7 for some reason. The wide-band (band 8) correlator caused 2 alarms but generally the data are of high quality. The weather was great, the water depth was even suitable for 1 mm project. I followed John Carpenter's reduction scripts. There were some problem with the noise source. Miriad generates too many spectra windows if there are frequency shifts in noise source integration. I followed suggestions from Marc Pound to flag some of the noise source integration, and it worked well. The "mosaic" option was used in "invert" to treat different primary beams. The "mossdi" command was used for the same reason, although the map looks noisier in the outer part due to the beam correction. The map was cleaned down to 4 sigma.

As a result, five molecules were detected, suprisingly. They are HCN, HCO^+, NH_2D, N_2H^+, CS. Figure 27 shows the spectra of N_2H^+ and HCO^+, and their moment 0 maps (contours) overlaid on N_2D^+ and DCO^+ moment 0 maps (from ALMA). The N_2H^+ moment 0 map (contour) was integrated over the velocity range of the central component. It is an overlap of many hyperfine stuctures which I'm not resolving or fitting here. As one can see, there are N_2H^+ and HCO^+ counterparts for the north core. The south core has relatively weaker N_2H^+ and HCO^+ emission. This probably indicates that G2-south has stronger deuteration level. But this is to be confirmed from my future calculation from chemical model.

Acknowledgement

The CARMA summer school is very helpful in radio interferometry. This experience is extremely treasured to me. I want to thank every instructor and every staff for their work and help. I want to also thank every classmate for sharing their ideas.

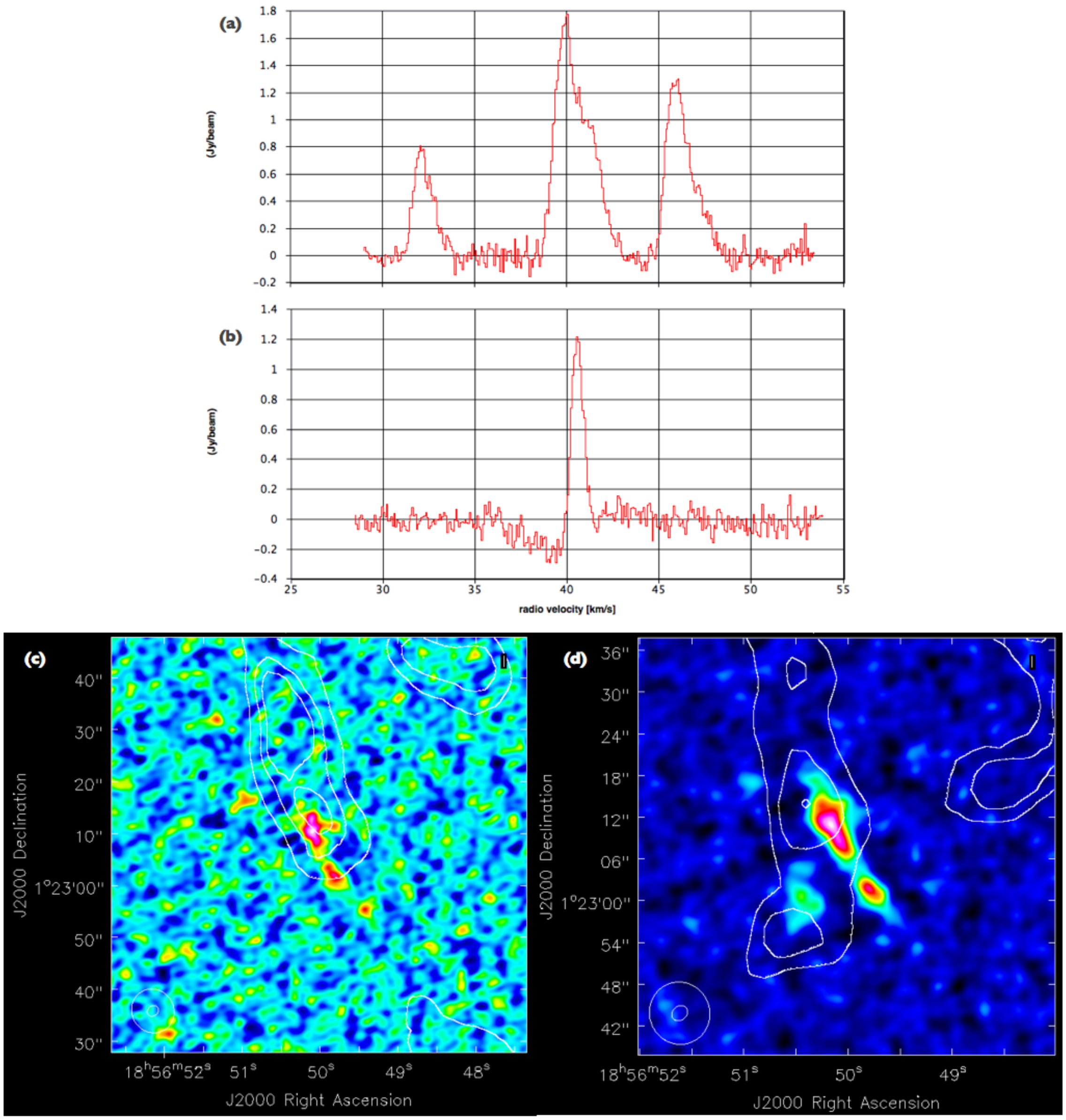

Fig. 27.—: (a) Sample spectrum of N_2H^+(1-0). (b) Sample spectrum of HCO^+(1-0). (c) Moment 0 contour of N_2H^+(1-0) overlaid on moment 0 raster map of N_2D^+(3-2) from ALMA. (d) Moment 0 contour of HCO^+(1-0) overlaid on moment 0 raster map of DCO^+(3-2) from ALMA.

9. The First CO map of Wolf-Rayet Barred Galaxy NGC 5430

Hsi-An Pan (Nobeyama Radio Observatory), Michiko Umei (Hokkaido University)

9.1. Introduction and Motivation

Wolf-Rayet (W-R) stars is an inhomogeneous population that they are very massive (initial mass > 30 M$_\odot$, can up to 80 M$_\odot$) and become an important constraint on the age of a starburst due to their short lifetime (Crowther 2007). W-R stars are often found in the irregular galaxies, blue compact dwarf galaxies, galaxy mergers, galactic center, and active galactic nuclei.

NGC 5430 (D = 43 Mpc, $1'' = 207$ pc, SB(s)b) is a strong-bar galaxy, located at $14^{\rm h}00^{\rm m}45\overset{\rm s}{.}7$ $+59^\circ19'42''$. The bar length is about $45''$, corresponding to $\sim$9 kpc. No apparent interaction is seen from its morphology (see Figure 28 upper left panel for the optical morphology, and upper right panel for the bar potential in K-band). Even though a circumnuclar starburst is ongoing at the nucleus as many barred galaxies, the brightest region in Hα image is $22''$ away from the center, residing in the leading side of the eastern bar (Figure 28 lower left panel). The brightest region is defined as a W-R region according to its spectral features (e.g., Fernandes et al. 2004). The W-R region in NGC 5430 contains 10^4 W-R stars and 10^5 O stars (Fernandes et al. 2004). The total star formation rate of the galaxy inferred from its infrared luminosity is $\sim$8 M$_\odot$ yr^{-1}. It is remarkable that it is relatively rare to see W-R region inhabiting in a bar. The reason is that the shocks generated by the orbit crowding of the gas in galactic bar tends to destroy compact/dense structure, and forbid the subsequent star formation. Therefore, NGC 5430 affords a chance to study the dynamical impact of a galactic bar on the star formation.

So far, NGC 5430 has been observed in ^{12}CO (1–0), ^{12}CO (2–1), ^{13}CO (2–1) and HCN (1–0) by IRAM 30-m telescope toward the center, and ^{12}CO (2–1) toward the bar (Kruegel et al. 1990; Contini et al. 1997). All of observations above were made with single pointing observation. Our CARMA map is the first, large scale CO map of this particular starburst galaxy.

9.2. Observation

The observation was carried out on July 30th, 2013 with a 5-hour track (LST 14 hr – 19 hr). CARMA-15 with E configuration was used. Three narrow bands (250 MHz) respectively center at ^{12}CO (1–0) (115.27 GHz) and its isotopic lines, ^{13}CO (1–0) (110.20 GHz) and C^{18}O (1–0) (109.78 GHz). Three wide bands (500 MHz) are placed between the frequency of ^{13}CO (1–0) and ^{12}CO (1–0) to check the continuum. The flux, passband, and phase calibrators are mwc349, 1635+381, and 1642+689, respectively. Total on source time is about 3 hours.

9.3. Results

The ^{12}CO channel map of NGC 5430 is displayed in Figure 29. The final angular resolution is $\sim 8''$ (1.7 kpc). Except for the galactic center, both eastern (e.g., 3058 km s^{-1}) and western (e.g., 2938 km s^{-1}) bar are clearly detected with about 5σ detection. The integrated intensity map is shown in the lower right panel of Figure 28. It is obvious from the intensity map that the molecular gas is concentrated at the center, as well as the leading side of the bar, presumably due to the orbit crowding of gas under a bar potential. The overall morphology of ^{12}CO map is consistent with other wavelengths in Figure 28. However, the W-R region in the bar does not have a corresponding peak in ^{12}CO image. The reason may be the insufficient resolution that the compact (and probably small) structures have been smoothed in the beam.

In order to estimate the missing flux originated from the short spacing problem, the integrated intensity map of ^{12}CO was convolved to a resolution of $22''$, corresponding to the beam size of IRAM 30-m telescope at 115 GHz (Kruegel et al. 1990). The missing flux is measured to be $\sim$16% in the central $22''$. In the bar region, there is no available single dish observation to estimate the missing flux in ^{12}CO (1–0), but it is common that the galactic disk has larger missing flux than the central region due to the larger amount of diffuse gas. For this reason, the missing flux in the bar region is likely $> 16\%$.

The isotopic line of ^{12}CO, ^{13}CO is also detected, but only at the galactic center since typically ^{13}CO has intensity 5 – 25 times lower than that of ^{12}CO (Paglione et al. 2001). The spectral profiles of central $8''$ (corresponds to the region of nuclear starburst) in both lines are shown in Figure 30 (^{12}CO/8 in black and ^{13}CO in red). Both lines show a two-peak profile with central velocity around 2970 km s^{-1}. The ^{12}CO[K]-to-^{13}CO[K] is about 16 in the galactic center, which is a typical number for a nuclear starburst (Paglione et al. 2001). No C^{18}O is detected in this observation.

9.4. Future Work

There are two things to be improved in the future. The first one is angular resolution. The current resolution is $8''$ or 1.6 kpc, which is significantly larger than the real size of CO emitter. The future CARMA observation with resolution $<3''$ will place the physical resolution down to a sub-kpc scale. Then we can compare the gas and star formation properties of NGC 5430 with those very nearby galaxies (e.g., Bigiel et al. 2008) under a compatible physical resolution.

Another issue is missing flux, they imply the existence of diffuse component. Diffuse gas may not directly involve to the star formation but they probably dominate the amount of molecular gas and reflect the gas dynamics in barred galaxies. It has been known that the gas motion can decide the location of massive star formation (Wozniak 2007). Therefore, to figure out the dynamical influence of galactic bar to the star formation and the formation of W-R region, missing flux is an important problem to fix. It can be fixed by single dish observation. A proposal of Nobeyama 45-m telescope is ready to submit by next deadline (Sep. 2013).

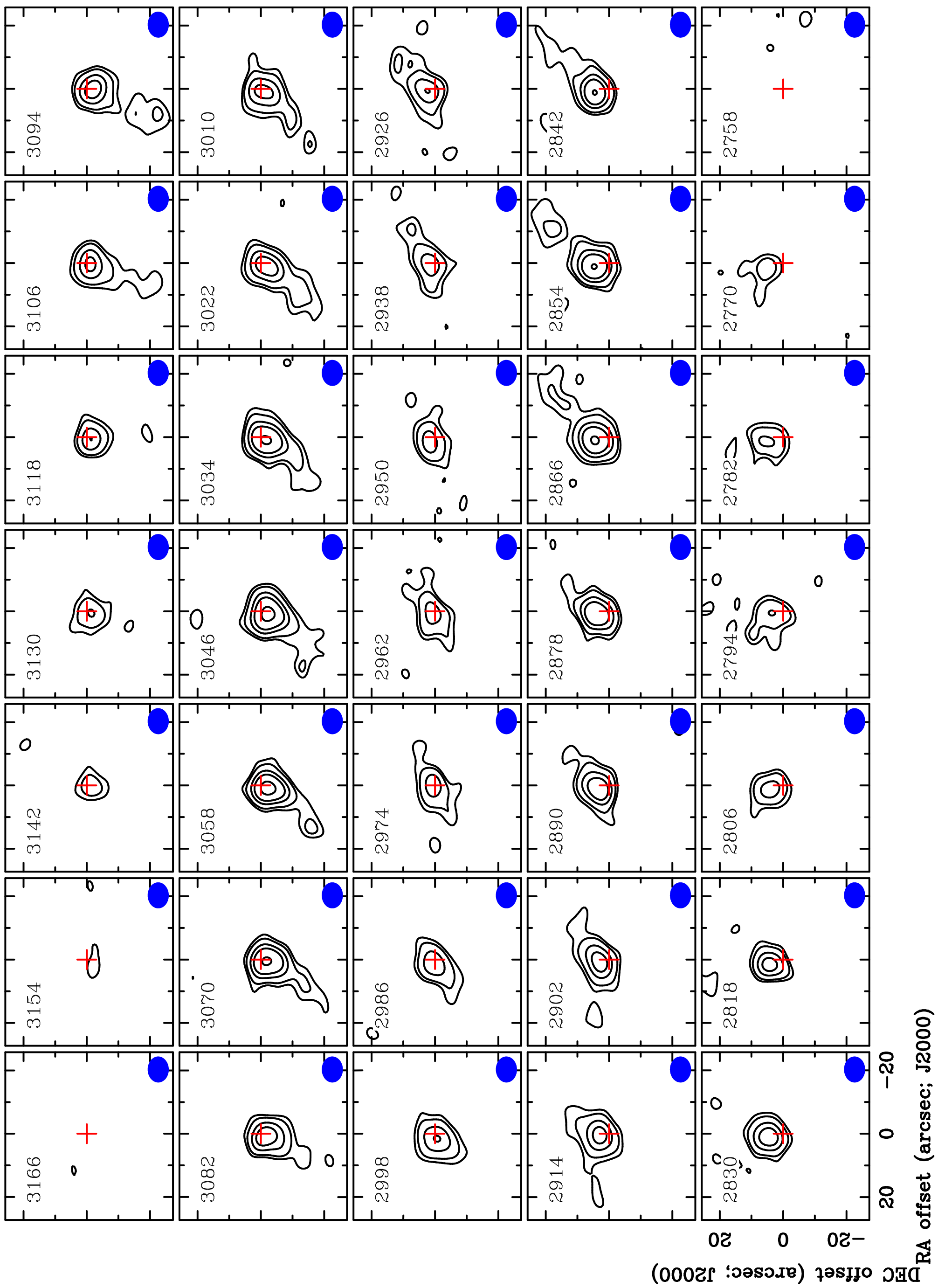

Fig. 28.—: Upper left: i-band image from Sloan Digital Sky Survey (SDSS). Upper right: K-band image from 2MASS. Lower left: Hα image from Epinat et al. (2008). Lower right: ^{12}CO (1-0) integrated intensity map from this work. The beam size of CO map is overlaid in the lower right of this panel. The green circle in each panel indicates the primary beam of CARMA, $\sim$60″ in diameter.

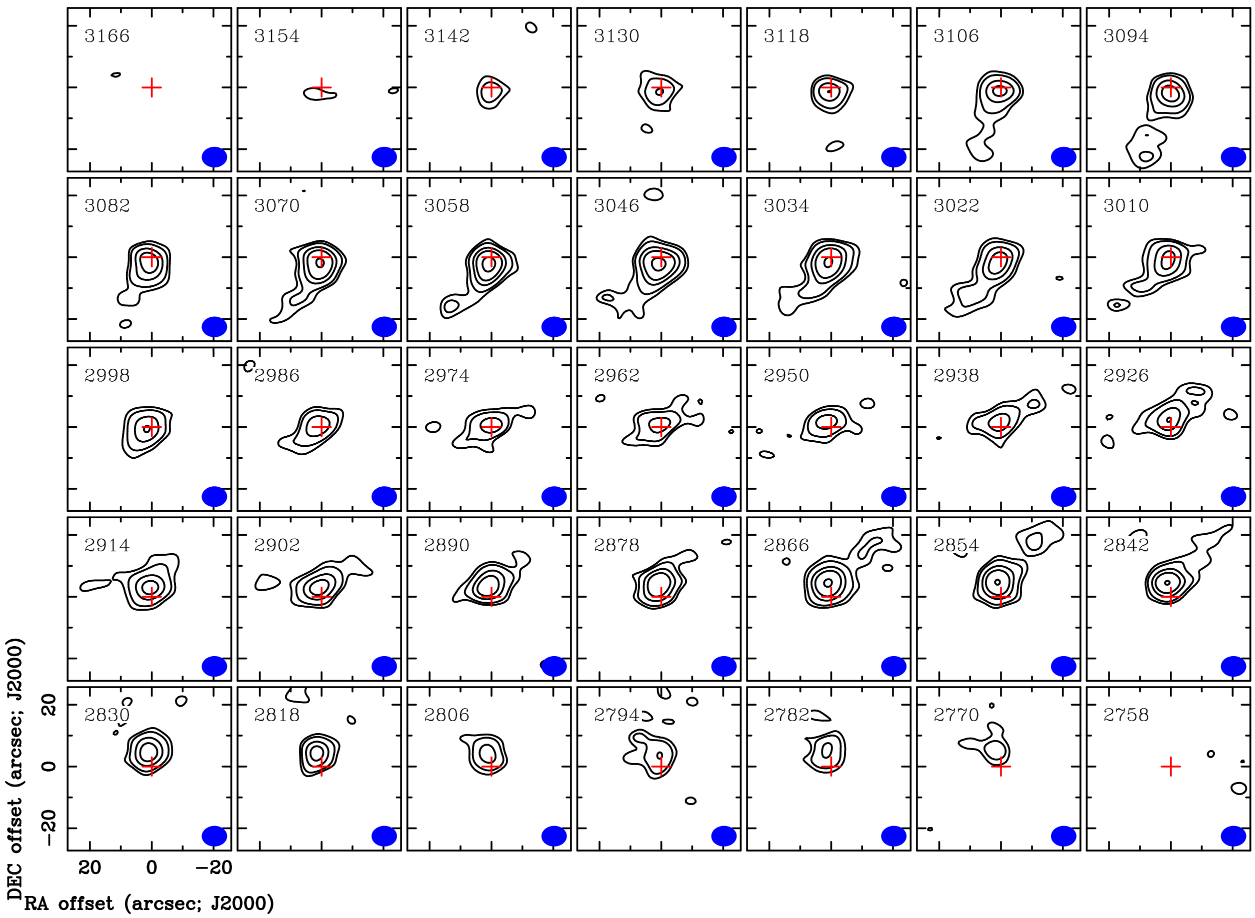

Fig. 29.—: Channel map of ^{12}CO (1-0). The contours are 3, 5, 10, 15, and 25 σ, where 1 σ is 25mJy beam^{-1}. The red cross indicates the galactic center of each channel. The beam size is overlaid at the bottom right.

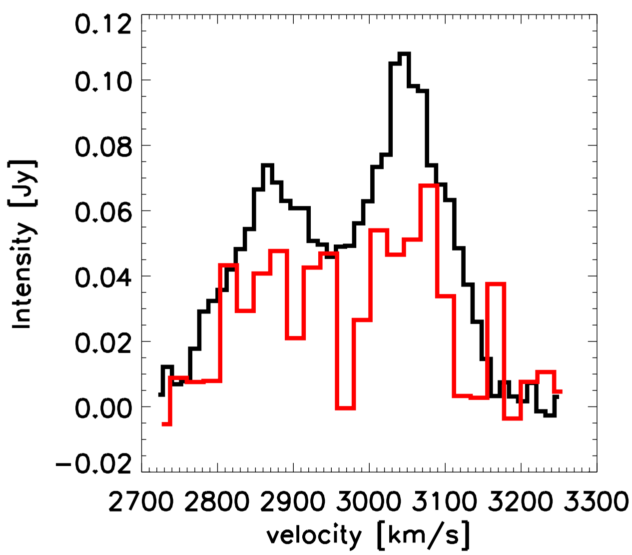

Fig. 30.—: The central spectrum of ^{12}CO in black and ^{13}CO in red. The flux of ^{12}CO has been divided by 8.

10. CARMA Observations of CO in the Galaxy Merger NGC 660

Stephen Clouse (UIUC) and Arnab Dhabal (UMD)

10.1. Introduction

NGC 660 is a polar ring galaxy merger that is 11 Mpc away with a recession velocity of 845 km s^{-1} (LSR). This is an interesting galaxy to study due to its unique structure. Most polar ring galaxy mergers appear as quiescent lenticular galaxies van Driel et al. (1995) whereas NGC 660 has a distinct ring-like disk structure. In van Driel et al. (1995), large scale H1 observations of NGC 660 clearly show this ring-like structure and small scale (12"-22" resolution) ^{12}CO and ^{13}CO observations show a small compact structure with a velocity spread of $\sim$500 km s^{-1}. Israel (2009) also observed the merger in ^{12}CO and ^{13}CO showing a rough position velocity diagram with little resolved detail. Our motivation for observing NGC 660 is to obtain 10" resolution images of the inner most 2' of the merger and to obtain spectra with 3 MHz resolution.

10.2. Observation and Reduction

From the spectral data in Israel (2009), NGC 660 has a velocity spread corresponding to a 192 MHz width. Thus, out of the eight windows in the Upper Side Band, we used three of them at 250 MHz centered at the ^{12}CO line, ^{13}CO line and C^{18}O line. For better spectral resolution, we also used two slightly overlapping 125 MHz windows on the ^{12}CO line. The remaining three windows with 500MHz width are used in the continuum away from the strong lines for calibration purposes.

For our observations we used the CARMA 15 array in the E configuration in 3-bit singular polarization mode. The primary beam size is 63". van Driel et al. (1995) showed that the ^{12}CO emission in NGC 660 extended beyond 1'. Therefore, a 7 point mosiac was used to cover the entire emission area. These previous observations show an observed flux of 400 mJy. In order to obtain a detectable signal in ^{12}CO, the source was observed for 5.6 hours.

The data collected was in the form of visibilities for different baselines. The UV data was checked for errors and appropriately flagged, then split into Wide (250 MHz, 500 MHz) and Narrow bands (125 MHz). Phase and amplitude offsets between the different windows were removed followed by flux and phase calibration. We invert the visibilities for the channels corresponding to the 250 MHz, ^{12}CO band to get the synthesized beam and image. To remove continuum emission and isolate the line emission, we invert the visibilities corresponding to the continuum bands and form a stacked image. We then subtracted the continuum emission from each of the frequency channels in our line data leaving only the ^{12}CO residual.

After removing the continuum emission, a deconvolution method is applied for imaging. Models for deconvolution were obtained by using both the SDI clean method and the Maximum Entropy method. This was done using the Miriad tasks 'mossdi' and 'mosmem' respectively. The pre-deconvolved model that we obtained using the SDI method was used as a starting point for the Maximum Entropy algorithm to ensure its convergence. The models obtained were used to deconvolve our synthesized images to get the final images using the Miriad task 'restor' These final images were used for data analysis (see Fig. 31).

10.3. Results and Conclusions

The ^{12}CO emission from the central region of NGC 660 was confirmed and imaging was done. This emission seems to be arising from only one of the pair of galaxies, which is edge on and inclined at about 45 degrees. The image does not cover the entire central region of the vertical galaxy as shown in Fig 32.

Our spectral analysis show that the velocity distribution has a double horned structure which matches very closely to that of van Driel et al. (1995). We conclude that the CO at the galaxy center has a high rotational velocity, contributing to the entire spectrum. This is also confirmed by a position-velocity map along the major axis of the galaxy (see Fig. 33).

A similar cspatial analysis was done on the ^{13}CO and C^{18}O, and spectral analysis averaging over similar image area as the ^{12}CO was also analyzed. Some structure was visible for ^{13}CO near the galaxy's center, and low line emission with similar velocity spread was noted as shown in the spectra in Fig. 34

A comparison of the results from the CLEAN and maximum entropy algorithms was carried out. Both of them agree to a high degree, but the same flux contour lines for the the SDI method are found to be enclosed by those produced by the Maximum Entropy Method as one might expect (see Fig. 35). This illustrates that the CLEAN method searches for point like structures unlike maximum entropy, which fits a model to the image which fits extended structures more accurately.

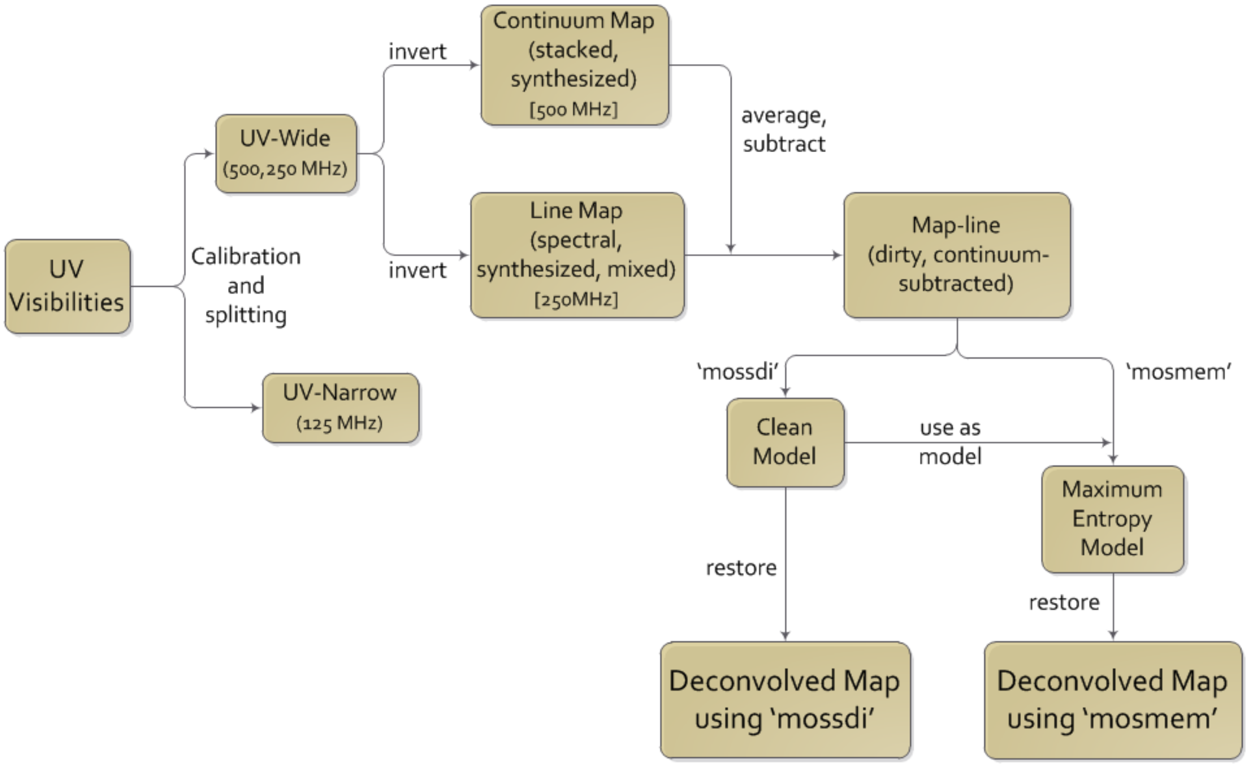

Fig. 31.—: This flowchart illustrates the reduction process producing images using both CLEAN and maximum entropy algorithms.

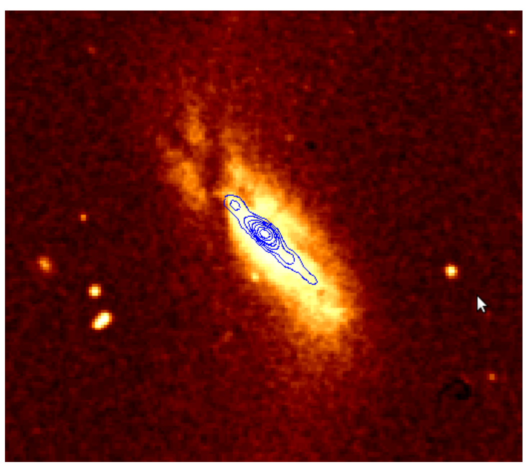

Fig. 32.—: This is an optical image (from SAO-DSS server) with millimeter contours of the ^{12}CO emission overlaid.

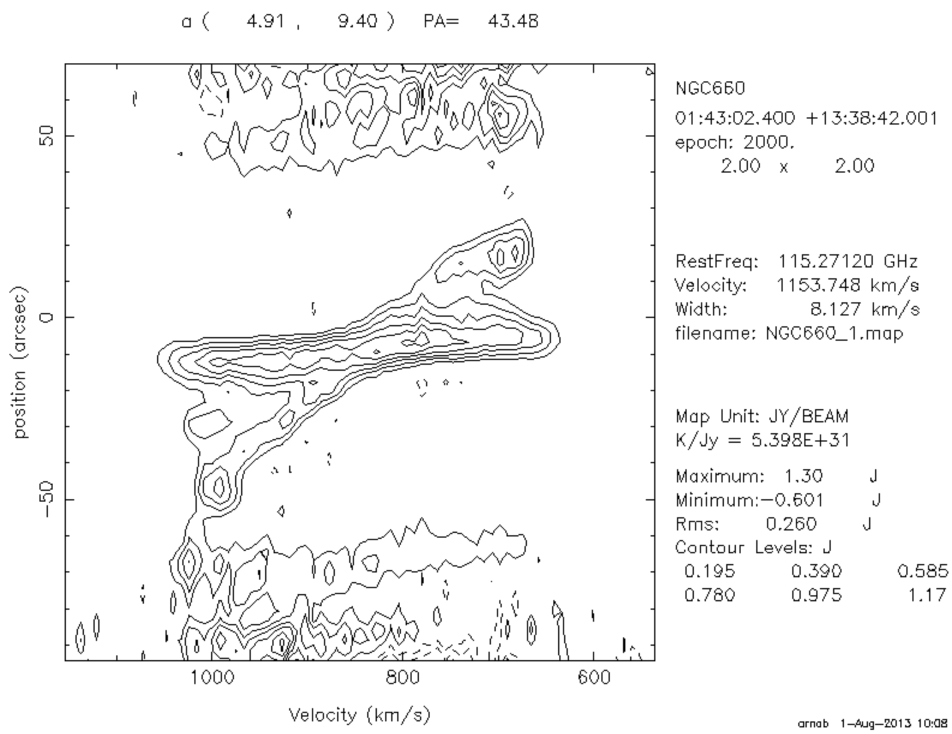

Fig. 33.—: A Position-Velocity plot of the ^{12}CO emission in NGC 660. As can be seen, the linear trend in the emission indicates solid body rotation.

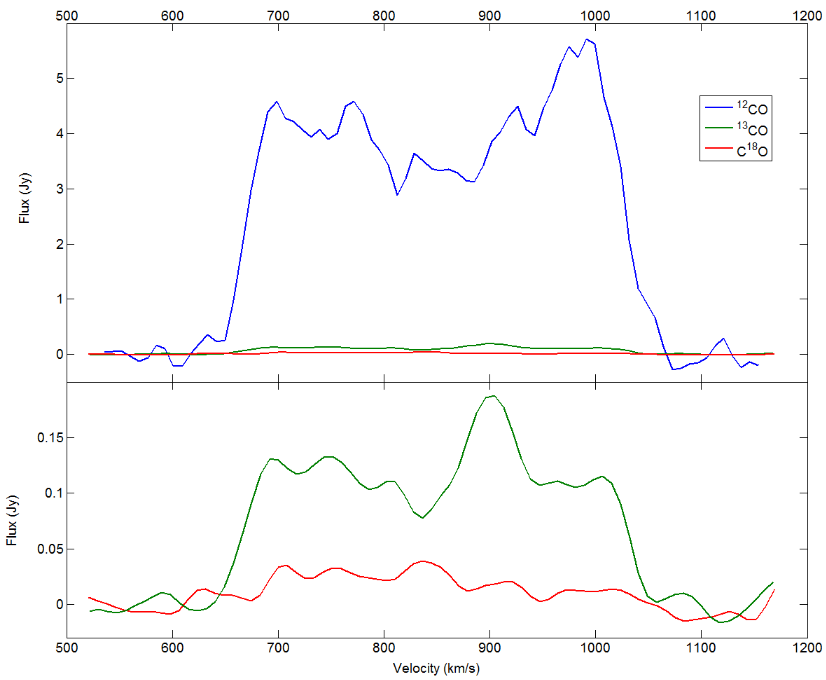

Fig. 34.—: This shows the spectra obtained by averaging over a region which encloses all the emission in NGC 660. A smaller region was selected for ^{13}CO and C^{18}O

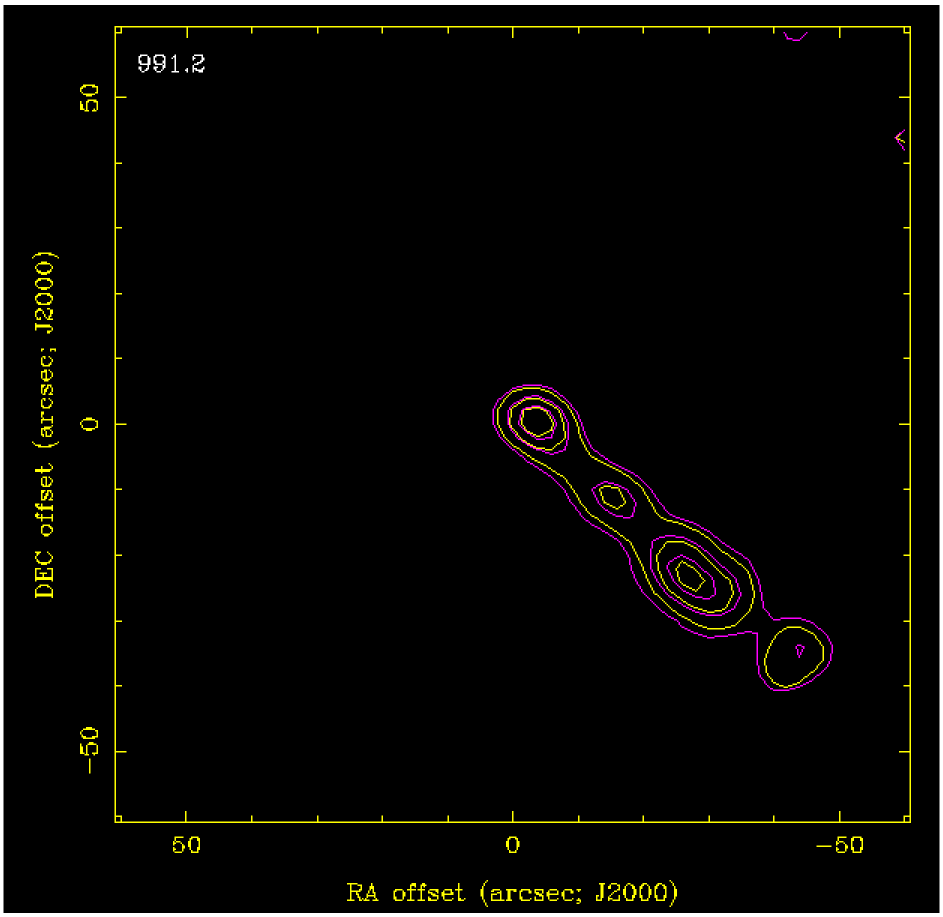

Fig. 35.—: Shown above are iso-contours of the models produced by the CLEAN and maximum entropy deconvolution algorithms used in Miriad. The yellow and magenta represent the models produced by tasks 'mossdi' and 'mosmem' respectively.

11. ^{12}CO(1-0) detection in Hickson Compact Group 96
Sandra Liss and Natalie Butterfield

11.1. Background and Motivation

Some of the biggest unanswered questions in astronomy center around what are collectively referred to as "origins": the formation and subsequent evolution of the objects in our Universe. In particular, understanding the early stages of star formation is essential for understanding topics ranging from planet formation to galaxy evolution. However, limitations in instrument resolution and sensitivity make it difficult to directly observe these high redshift processes. One way to address these obstacles is to observe local analogs of the early Universe environments. Compact groups (CGs) are an ideal example of these low redshift analogs; the high number density and low velocity dispersions of CGs lead to frequent prolonged galaxy interactions similar to those in the early universe allowing us to probe the conditions of star formation in the early Universe.

Hickson compact group (HCG) 96 is one such compact group (see Figure 36). At a redshift of 0.0292, it is located approximately 115 Mpc away from the Milky Way. HCG 96 has four members, the relevant properties of which are listed in Table 3. Previous multiwavelength observations of HCG 96 indicate that it is an excellent candidate for CO mapping; mid-infrared observations suggest that 96a is actively forming stars, and that 96c and 96d may also have regions of active star formation (Walker et al. (2012)). This is supported by complementary HI mapping (see Figure 37), which shows HI associated with all three of these galaxies, particularly with 96a (Verdes-Montenegro et al. (2001)).

Single dish observations of CO in HCG 96 have been reported by Verdes-Montenegro et al. (1998) with the NRAO 12m telescope at Kitt Peak and Leon et al. (1998) with the IRAM 30m dish. Both groups detect CO in 96a and 96c (see Figure 38). For 96a, Verdes-Montenegro report a peak brightness temperature of 31.8 mK with a line width of 251 km s^{-1}, while Leon et al. found a brightness temperature of 116.5 mK and a line width of 192 km s^{-1}. For 96c, Verdes-Montenegro et al. and Leon et al. report brightness temperatures of 5.7 mK and 11.6 mK, and line widths of 92 km s^{-1}and 320 km s^{-1}, respectively.

For our CARMA summer school project, we observed the ^{12}CO(1-0) transition in HCG 96 in order to map its CO content.

11.2. Observations and Data Reduction

Observations presented in this memo were made with the Combined Array for Research at Millimeter Array (CARMA) on July 30th 2013 in the 3mm band. Due to the two different size dishes in the CARMA15 array we had three different size primary beams - 64″ and 115″, corresponding to the 10m and 6m dishes respectively, and a hybrid beam with a size of 83″. Since no beam was large enough to fully cover HCG 96 with an angular diameter of 138″, we had to mosaic the group

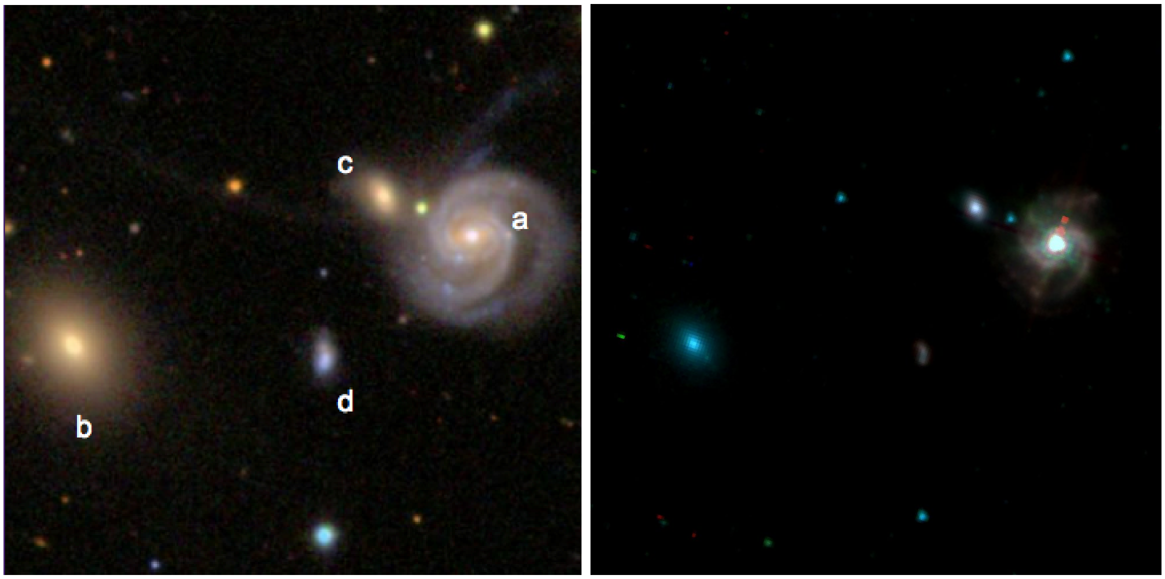

Fig. 36.—: Previous observations of HCG 96: (a) Three color image of HCG 96 using SDSS u, g, and r bands. The four members of the group are labeled in white. Blue indicates regions of star formation. (b) Three color MIR image of HCG 96 from Spitzer. Here, red indicates active star formation.

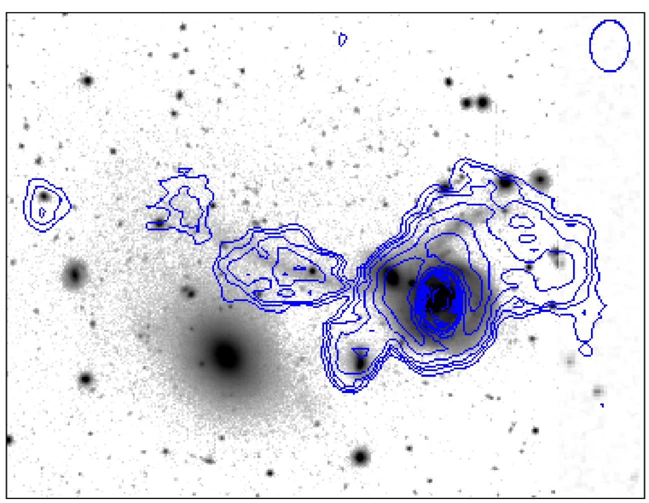

Fig. 37.—: Previous HI observations of HCG 96 show that 96a, 96c and 96d have HI content (Verdes-Montenegro et al. (1998)). The lack of HI emission associated with 96b informed our mosaic pointings.

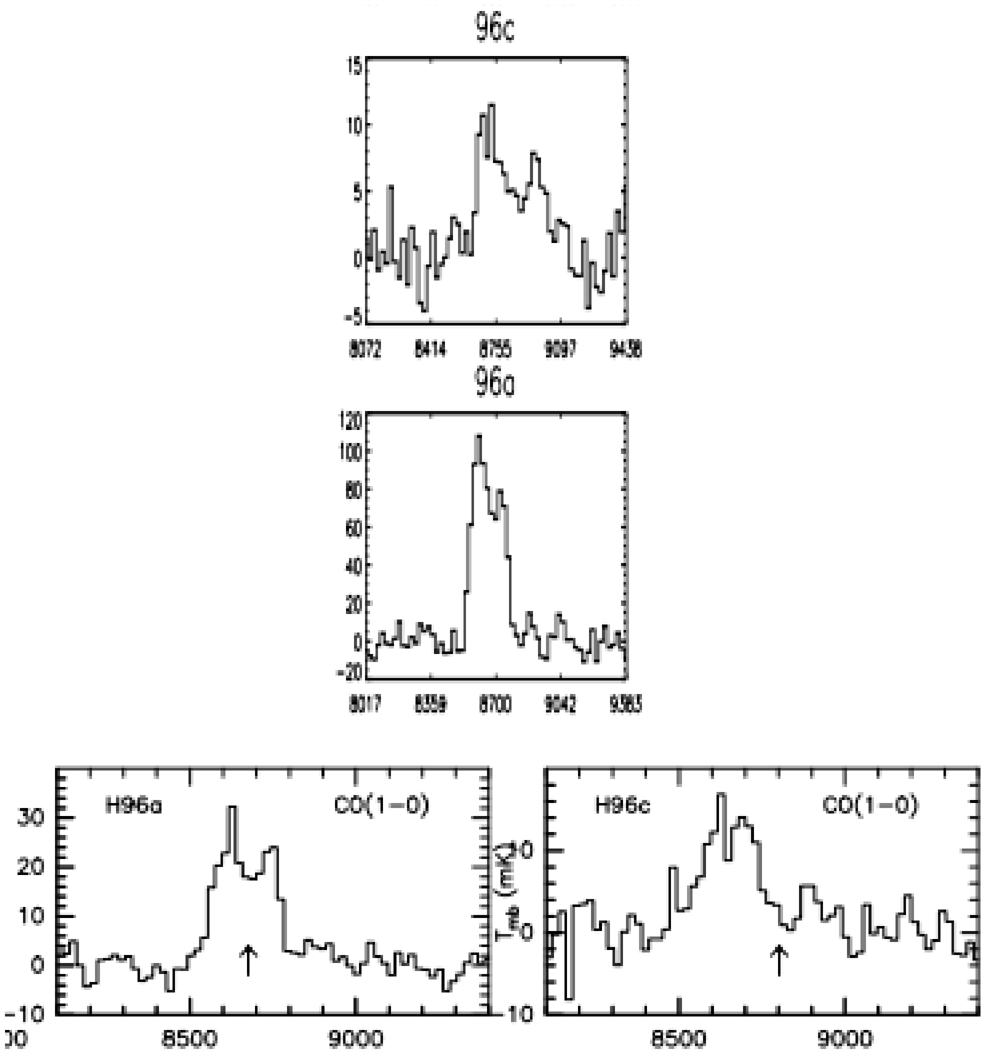

Fig. 38.—: Previous single dish observations of the ^{12}CO(1-0) transition in HCG 96 by (a) Leon et al. (1998) with the IRAM 30m and (b) Verdes-Montenegro et al. (1998) with the Kitt Peak 12m. The y-axis for both sets of data is in mK. The x-axis is in units of km s^{-1}.

Table 3:: HCG 96 Members

Group Member	**Morphology**	**v$_{LSR}$ (km s^{-1})**
a	SAbc	8675
b	E2	8620
c	Sa	8856
d	Im	8979

for our observation (see Figure 39). To get enough time on source for each pointing we were limited to 8 pointings over our 5 hour observing block. Also in the interest of time on source, we mosaicked with a 1/4 primary beam overlap instead of the traditional 1/2 primary beam Nyquist sampling. The total time we spent per pointing was $\sim$ 23 minutes.

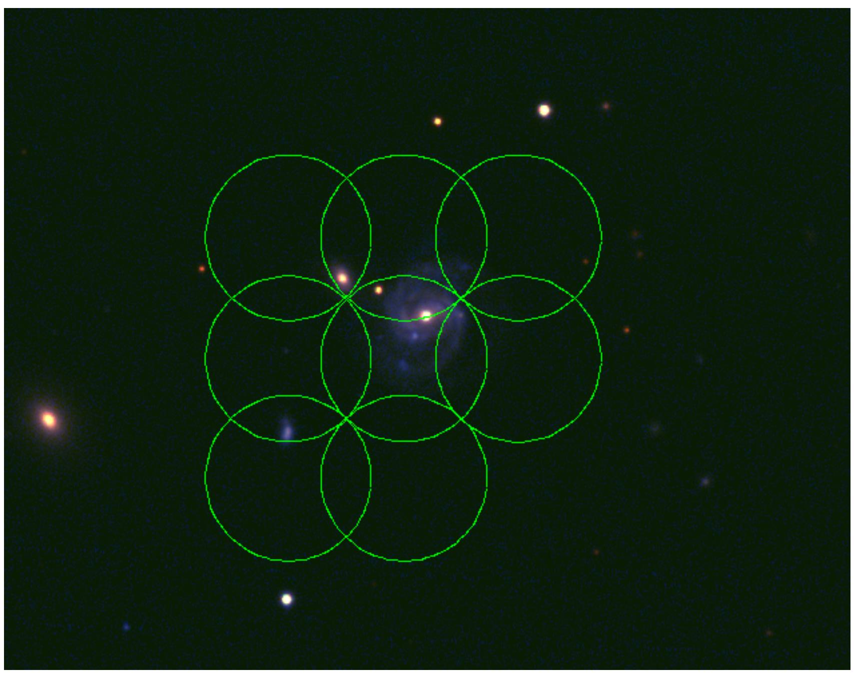

Fig. 39.—: Our 8-pointing mosaic of HCG 96 using the smallest beam size, which corresponds to the 10 meter dishes. The mosaicked field included 96a, 96c, and 96d.

For these observations we used mwc349 was our flux calibrator and 3c454.3 as our gain calibrator. Because 3c454.3 was so bright, we were able to use the same data for our passband calibration. We performed all of the primary routine calibration steps using a basic data reduction script provided by John Carpenter. After performing these initial calibrations we used the programs miriad, CASA, and ds9 to reduce, display, and analyze the data. In order to cover the entire velocity space of the group (see Table 3), we used two overlapping bands to cover each spectral window of interest.

When imaging, we therefore combined the two windows that included the ^{12}CO(1-0) transition data in velocity space rather than channel space. After using MOSSDI to clean the data, we re-imaged the data for analysis.

11.3. Analysis and Conclusions

Stepping through our data cube revealed two distinct CO sources separated in both physical and velocity space. The peak intensity map, shown in the right panel of Figure 40 shows these two sources and their structure. The left panel shows where the CO sources correspond to in the optical image; the sources appear on either side of the bulge at the center of 96a. The sources were measured to have an angular separation of 14″, which, at the distance of HCG96, corresponds to a physical separation of approximately 7.8 Kpc. Our observations showed a peak intensity of approximately 0.5 Jy beam^{-1}. This value is approximately several mK, which is on the order of the previous single dish detections.

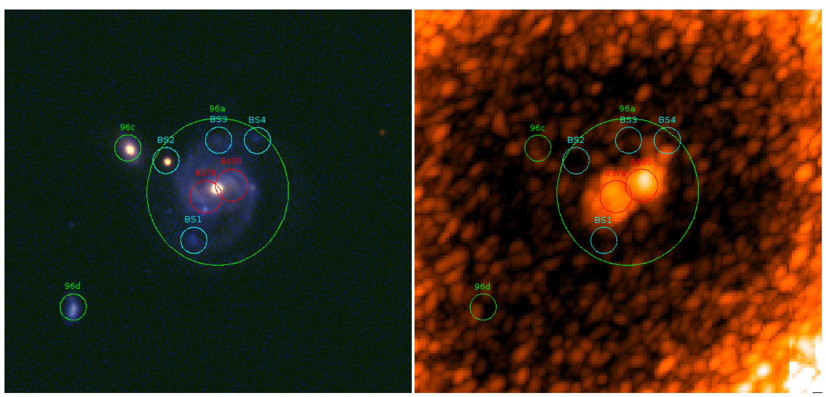

Fig. 40.—: A side-by-side comparison of the SDSS optical image and our ^{12}CO CARMA detections. The green circles in both panels show the location of the group galaxies, the cyan show interesting optical sources, and the red show our two CO sources.

The sources are separated in velocity by 130 km s^{-1}, with the left source showing a blue-shifted velocity relative the the galaxy's v_{LSR} and the right source showing a red-shifted one. This structure is also evident in the moment 1 map (see Figure 41). The moment 1 map shows signs of rotation, consistent with 96a's rotation. The moment 2 map indicates that this rotation is smooth through the galaxy's center. Though 96a appears face-on, this suggest that it is slightly inclined.

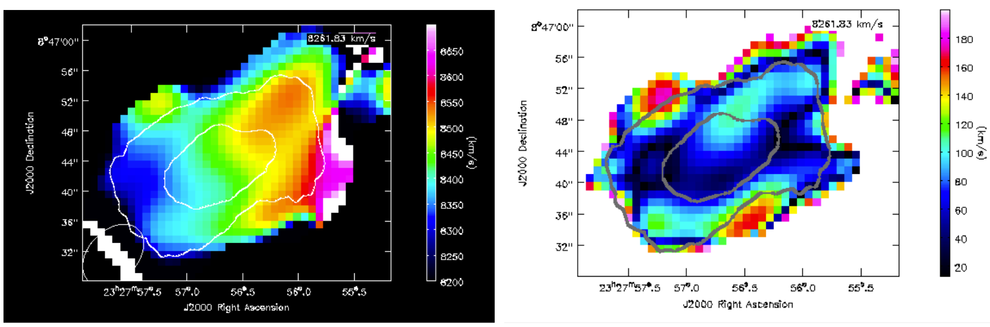

Fig. 41.—: The moment 1 and moment 2 maps of HCG 96, with moment 0 contours overlaid.

E-mail addresses

Melodie Kao (Caltech), mkao@astro.caltech.edu
Gina Duggan (Caltech), ginaeduggan@gmail.com
Ben Tofflemire (Wisconsin), tofflemi@astro.wisc.edu
Melissa Louie (SUNY, Stony Brook), melissa.louie@stonybrook.edu
Rosalie McGurk (UC, Santa Cruz), rmcgurk@ucsc.edu
Hsi-An Pan (GUAS/NRO), pan.h.a@nao.ac.jp
Sandy Liss (Virginia), sel7pa@virginia.edu
Emma Yu (Texas), moyu@astro.as.utexas.edu
Jesus Rivera (Rutgers), jrivera@physics.rutgers.edu
Stephen Clouse (Illinois), clouse2@illinois.edu
Michiko Umei (Hokkaido), umei@astro1.sci.hokudai.ac.jp
Alfred Tiley (Oxford), alfietiley@gmail.com
Moumita Aich (KwaZulu-Natal), aich@ukzn.ac.za
Anna Miotello (Leiden), annina.mio@gmail.com
Shuo Kong (Florida), skong@astro.ufl.edu
Nina Van der Pyl (Bristol), nina.vanderpyl@bristol.ac.uk
Arnab Dhabal (Maryland), adhabal@astro.umd.edu
Sam Kim (PUC), skim@astro.puc.cl
Yixian Cao (Illinois), ycao17@illinois.edu
Katherine de Kleer (UC, Berkeley), kdekleer@berkeley.edu
Natalie Butterfield (Iowa), natalie-butterfield@uiowa.edu

REFERENCES

Andreon, S., & Hurn, M. A. 2010, MNRAS, 404, 1922

Bigiel, F., Leroy, A., Walter, F., Brinks, E., de Blok, W. J. G., Madore, B., & Thornley, M. D. 2008, AJ, 136, 2846

Bonnell, I. A., Clarke, C. J., Bate, M. R., & Pringle, J. E. 2001, MNRAS, 324, 573

Butler, M. J., & Tan, J. C. 2009, ApJ, 696, 484

—. 2012, ApJ, 754, 5

Carlstrom, J. E., Holder, G. P., & Reese, E. D. 2002, ARA&A, 40, 643

Colwell, J. E., & et al. 2007, Icarus, 190, 127

Contini, T., Wozniak, H., Considere, S., & Davoust, E. 1997, A&A, 324, 41

Crowther, P. A. 2007, ARA&A, 45, 177

Dalgarno, A., & Lepp, S. 1984, ApJ, 287, L47

Ebeling, H., Barrett, E., & Donovan, D. 2004, ApJ, 609, L49

Ebeling, H., Barrett, E., Donovan, D., Ma, C.-J., Edge, A. C., & van Speybroeck, L. 2007, ApJ, 661, L33

Ebeling, H., Edge, A. C., & Henry, J. P. 2001, ApJ, 553, 668

Eckart, A., Cameron, M., Jackson, J. M., Genzel, R., Harris, A. I., Wild, W., & Zinnecker, H. 1991, ApJ, 372, 67

Edge, A. C., Ebeling, H., Bremer, M., Röttgering, H., van Haarlem, M. P., Rengelink, R., & Courtney, N. J. D. 2003, MNRAS, 339, 913

Epinat, B., Amram, P., & Marcelin, M. 2008, MNRAS, 390, 466

Fernandes, I. F., de Carvalho, R., Contini, T., & Gal, R. R. 2004, MNRAS, 355, 728

Fontani, F., et al. 2011, A&A, 529, L7

Grossman, A. W., Muhleman, D. O., & Berge, G. L. 1989, Science, 245, 1211

Hogerheijde, M. R., van Dishoeck, E. F., Blake, G. A., & van Langevelde, H. J. 1998, ApJ, 502, 315

Israel, F. P. 2009, A&A, 506, 689

Kennicutt, Jr., R. C., et al. 2003, PASP, 115, 928

Kruegel, E., Chini, R., & Steppe, H. 1990, A&A, 229, 17

Kuno, N., et al. 2007, PASJ, 59, 117

LaRoque, S. J., Bonamente, M., Carlstrom, J. E., Joy, M. K., Nagai, D., Reese, E. D., & Dawson, K. S. 2006, ApJ, 652, 917

Leon, S., et al. 2007, A&A, 473, 747

Ma, C.-J., Ebeling, H., & Barrett, E. 2009, ApJ, 693, L56

Ma, C.-J., Ebeling, H., Donovan, D., & Barrett, E. 2008, ApJ, 684, 160

McKee, C. F., & Tan, J. C. 2003, ApJ, 585, 850

Mroczkowski, T., et al. 2012, ApJ, 761, 47

Paglione, T. A. D., et al. 2001, ApJS, 135, 183

Pyo, T.-S., et al. 2005, ApJ, 618, 817

Rathborne, J. M., Jackson, J. M., & Simon, R. 2006, ApJ, 641, 389

Regan, M. W., Sheth, K., Teuben, P. J., & Vogel, S. N. 2002, ApJ, 574, 126

Roberts, W. W. 1969, ApJ, 158, 123

Sault, R. J., Teuben, P. J., & Wright, M. C. H. 1995, in Astronomical Society of the Pacific Conference Series, Vol. 77, Astronomical Data Analysis Software and Systems IV, ed. R. A. Shaw, H. E. Payne, & J. J. E. Hayes, 433

Scoville, N. Z., & Solomon, P. M. 1974, ApJ, 187, L67

Swift, J. J., Welch, W. J., & Di Francesco, J. 2005, ApJ, 620, 823

Tan, J. C., Kong, S., Butler, M. J., Caselli, P., & Fontani, F. 2013, ArXiv e-prints

van Driel, W., et al. 1995, AJ, 109, 942

van Weeren, R. J., Röttgering, H. J. A., Brüggen, M., & Cohen, A. 2009, A&A, 505, 991

Verdes-Montenegro, L., Yun, M. S., Perea, J., del Olmo, A., & Ho, P. T. P. 1998, ApJ, 497, 89

Verdes-Montenegro, L., Yun, M. S., Williams, B. A., Huchtmeier, W. K., Del Olmo, A., & Perea, J. 2001, A&A, 377, 812

Walker, L. M., Johnson, K. E., Gallagher, S. C., Charlton, J. C., Hornschemeier, A. E., & Hibbard, J. E. 2012, AJ, 143, 69

Wang, P., Li, Z.-Y., Abel, T., & Nakamura, F. 2010, ApJ, 709, 27

Weiland, J. L., & et al. 2011, ApJS, 192, 19

Wozniak, H. 2007, A&A, 465, L1